Advances in Pantographic Structures: Design, Manufacturing, Models, Experiments and Image Analyses

Francesco dell'Isola · Piere Seppecher · Mario Spagnuolo · Emilio Barchiesi · François Hild · Tomasz Lekszycki · Ivan Giorgio · Luca Placidi · Ugo Andreaus · Massimo Cuomo · Simon R. Eugster · Aron Pfaff · Klaus Hoschke · Ralph Langkemper · Emilio Turco · Rizakan Sarikaya · Aviral Misra · Michele De Angelo · Francesco D'Annibale · Amine Bouterf · Xavier Pinelli · Anil Misra · Boris Desmorat · Marek Pawlikowski · Corinne Dupuy · Daria Scerrato · Patrice Peyre · Marco Laudato · Luca Manzari · Peter Göransson · Christian Hesch · Sofia Hesch · Patrick Franciosi · Justin Dirrenberger · Florian Maurin · Zacharias Vangelatos · Costas Grigoropoulos · Vasileia Melissinaki · Maria Farsari · Wolfgang Muller · Emek Abali · Christian Liebold · Gregor Ganzosch · Philip Harrison · Rafał Drobnicki · Leonid Igumnov · Faris Alzahrani · Tasawar Hayat

F. dell'Isola
International Research Center M&MoCS, Università degli Studi dell'Aquila, L'Aquila, Italy
Dipartimento di Ingegneria Civile, Edile-Architettura e Ambientale, Università degli Studi dell'Aquila, L'Aquila, Italy
Research Institute for Mechanics, National Research Lobachevsky State University of Nizhni Novgorod, Nizhny Novgorod, Russia
NAAM Research Group, Department of Mathematics, King Abdulaziz University, Jeddah 21589, Saudi Arabia

P. Seppecher
Institut de Mathématiques de Toulon, Université de Toulon, Toulon, France

M. Spagnuolo

CNRS, LSPM UPR3407, Université Paris 13, Sorbonne Paris Cité, 93430 Villetaneuse, France
International Research Center M&MoCS, Università degli Studi dell'Aquila, L'Aquila, Italy
E-mail: mario.spagnuolo@lspm.cnrs.fr

E. Barchiesi · I. Giorgio · U. Andreaus
Dipartimento di Ingegneria Strutturale e GeotecnicaUniversità degli Studi di Roma "La Sapienza", Rome, Italy
International Research Center M&MoCS, Università degli Studi dell'Aquila, L'Aquila, Italy

F. Hild · A. Bouterf · X. Pinelli
Laboratoire de Mécanique et Technologie (LMT), ENS Paris-Saclay/CNRS/Université Paris-Saclay, 61 avenue du Président Wilson, 94235 Cachan Cedex, France

T. Lekszycki
Warsaw University of Technology, Warsaw, Poland
Department of Experimental Physiology and Pathophysiology, Medical University of Warsaw, Warsaw, Poland

L. Placidi
International Telematic University Uninettuno, Rome, Italy
International Research Center M&MoCS, Università degli Studi dell'Aquila, L'Aquila, Italy

M. Cuomo
Dipartimento di Ingegneria Civile e Architettura (DICAR)Università degli Studi di Catania, Catania, Italy

S. R. Eugster
Institute for Nonlinear Mechanics, University of Stuttgart, Stuttgart, Germany

A. Pfaff · K. Hoschke · R. Langkemper
Fraunhofer Institute for High-Speed Dynamics, Ernst-Mach-Institut, EMI, Ernst-Zermelo-Str. 4, 79104 Freiburg, Germany

E. Turco
Department of Architecture, Design and Urban Planning (DADU), University of Sassari, Alghero, Italy

R. Sarikaya
Mechanical Engineering (ME), The University of Kansas, Lawrence, USA

A. Misra
Blue Valley High School, 6001 159th St, Stilwell, Kansas, USA

M. De Angelo
Dipartimento di Ingegneria Civile, Edile Architettura e Ambientale (DICEAA), Università degli Studi dell'Aquila, L'Aquila

F. D'Annibale
International Research Center M&MoCS, Università degli Studi dell'Aquila, L'Aquila, Italy

A. Misra
Civil, Environmental and Architectural Engineering Department, University of Kansas, Lawrence, KS, United States

B. Desmorat
UMPC Université Paris 06, CNRS, UMR 7190, Institut d'Alembert, Sorbonne Université, Paris Cedex 05, France
Université Paris Sud 11, Orsay, France

M. Pawlikowski
Institute of Mechanics and Printing, Warsaw University of Technology, Warsaw, Poland

D. Scerrato
International Research Center M&MoCS, Università degli Studi dell'Aquila, L'Aquila, Italy

P. Peyre · C. Dupuy · J. Dirrenberger
Laboratoire PIMM, Arts et Métiers-ParisTech, CNRS, Cnam, 151 bd de l'Hôpital, 75013 Paris, France

M. Laudato
Dipartimento di Ingegneria e Scienze dell'Informazione e Matematica, Università degli Studi dell'Aquila, Coppito, Italy
International Research Center M&MoCS, Università degli Studi dell'Aquila, L'Aquila, Italy

L. Manzari · P. Göransson
KTH Royal Institute of Technology, Marcus Wallenberg Laboratory for Sound and Vibration Research, Stockholm, SE-100 44, Sweden

C. Hesch
Chair of Computational Mechanics, University of Siegen

S. Hesch
Chair of Product Development, University of Siegen

P. Franciosi
CNRS, LSPM UPR3407, Université Paris 13, Sorbonne Paris Cité, 93430 Villetaneuse, France

F. Maurin
DMMS Lab Flanders Make, Leuven, Belgium

Z.Vangelatos · C. Grigoropoulos
Department of Mechanical Engineering, University of California, Berkeley, California 94720, USA
Laser Thermal Laboratory, Department of Mechanical Engineering, University of California, Berkeley, California 94720, USA

V. Melissinaki · M. Farsari
Institute of Electronic Structure and Laser (IESL), Foundation of Research and Technology, Hellas (FORTH), Heraklion 70013, Crete, Greece

Abstract In the last decade the exotic properties of pantographic metamaterials have been investigated and different mathematical models (both discrete or continuous) have been introduced. In a previous publication a large part of the already existing literature about pantographic metamaterials has been presented. In this paper we give some details about the next generation of research in this field. We present an organic scheme of the whole process of design, fabrication, experiments, models and image analyses.

Keywords Pantographic Structures · Additive Manufacturing · Tomography · Generalised Continua · Digital Image Correlation

1 Introduction

Along the history of science, the efforts for developing models giving a description of some phenomena have always been triggered by the effective possibility to produce experimental evidences. In line with this methodology, Cauchy's version of Continuum Mechanics had a very large number of validations. The classical Continuum Mechanics contains some unnatural, hand-crafted, limitations to the choice of the terms which have to be considered in the energy of a deformable body [1,2]. In particular, it is decided *a priori* that only first gradients of displacement must be contained in the deformation energy. If this choice can be accepted without any other proof apart from the experimental validation for standard materials, it is not understandable why a similar approach should be adopted in any other case.

For example, it has been shown by Germain [3,4], Mindlin *et al.* [5–7], Toupin [8] and Sedov [9] how the presence of a microstructure can be described

W. Muller · . E. Abali · G. Ganzosch · C. Liebold
Faculty of Mechanics, Berlin University of Technology, Einsteinufer 5, 10587 Berlin, Germany

P. Harrison
School of Engineering, University of Glasgow, University Avenue, Glasgow, G12 8QQ, UK

R. Drobnicki
Dipartimento di Ingegneria e Scienze dell'Informazione e Matematica, Università degli Studi dell'Aquila, L'Aquila, Italy

L. Igumnov
Research Institute for Mechanics, National Research Lobachevsky State University of Nizhni Novgorod, Nizhny Novgorod, Russia

F. Alzahrani · T. Hayat
NAAM Research Group, Department of Mathematics, King Abdulaziz University, Jeddah 21589, Saudi Arabia

from a macroscopic point of view by introducing a second gradient (or strain gradient, as it was first called) term in the energy of the microstructured material [10–13].

The main criticism to higher gradient models was the following. If we have two models, both working, describing the same system, the simplest one should be preferred. In Ref. [14] it has been shown how the design of pantographic metamaterials [15] has been performed in order to obtain a material whose first gradient energy is zero. Pantographic metamaterials are, then, naturally described by a second gradient continuum model. The validation of this generalized model calls for the practical production of samples to use in experiments. Up to the last decade this was very difficult (see Fig. 1 for the fabrication of a pantographic structure. It was presumably not possible to simply fabricate it the "old" way). In the last years, the fast development of 3D printing technologies has improved the current possibilities of production of very small samples. It is now possible to fabricate a microstructured material by Additive Manufacturing [16].

This paper deals with an aspect of pantographic fabrics that is complementary and, by all the ways, correlated to that treated in Ref. [14]. Herein we put our focus on manufacturing techniques and processing that have been used so far to obtain pantographic structures. The paper is divided as follows: (i) design; (ii) manufacturing; (iii) modeling (short recalling); (iv) experimental results; (v) from data acquisition to discrete modeling. In order to give an idea of the complex and integrated procedure needed to study pantographic fabrics using the most advanced tools (including Lagrangian mechanics), the following workflow has been implemented: computer-aided design, acquisition of the CAD model into 3D printing workflow, experiments, analysis of experimental results via Digital Image Correlation (DIC).

2 Design and Manufacturing

The design of pantographic structures has been motivated in Ref. [14]. The fundamental idea was to design a metamaterial whose deformation energy is, at the first order, a second gradient energy. As an analogy with the beam deformation energy [17,18], it was proposed, as fundamental cell of the microstructure to be homogenized to get a second gradient macro model, a fiber network called pantographic beam [19], which has the following properties:

i. it is made of by two families of mutually orthogonal beams, intersecting by means of some cylinders called pivots (see Fig. 1);
ii. the pivots, in theory, have no torsional energy;
iii. an elongation of the structure corresponds (at the first order) to bending of the fibers, which is represented by a second gradient energy.

As a result of points (i)-(iii) the homogenized model corresponding to the pantographic beam has at the first order a deformation energy that is purely second gradient.

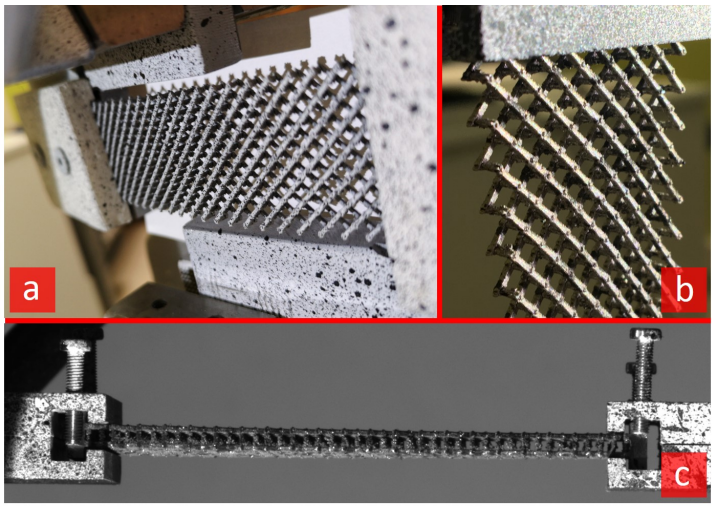

Fig. 1: Three different views of a metallic pantographic structure with perfect pivots

Thanks to the last advancements of the 3D printing technology, it is now possible to validate the model developed to describe pantographic metamaterials. With the computer-aided manufacturing technology it is possible to fabricate specimens whose geometrical structure can be controlled very precisely.The possibility to specify a design and manufacture an object by means of a software has far reaching consequences to experimental as well as numerical investigations. The production process consists of two steps: (i) computer-aided design, and (ii) additive manufacturing. The samples are produced with different geometrical properties, as well as different base materials (e.g. polyamide, steel, aluminum).

2.1 Design of Pantographic Structures

An appealing feature of computer aided design and additive manufacturing is baed upon the fact that exactly the same geometry can be used for both manufacturing and full-scale 3D numerical simulations. In Figs. 3-5 some of the currently designed (and CAD modeled) structures are shown. First, a pantographic beam (Fig. 2) has been introduced in the very first study about pantographic structures [19]. Notwithstanding it has been the first theoretically designed structure, it has been necessary to wait for the growth of the know-how in the CAD modeling and additive manufacturing of pantographic structures, due to the need for accuracy.

A pantographic structure with perfect pivots is shown in Fig. 3. In this case, the CAD modeling of this structure has been performed only recently, even though in the first works about pantographic structures [20,19] the pivots

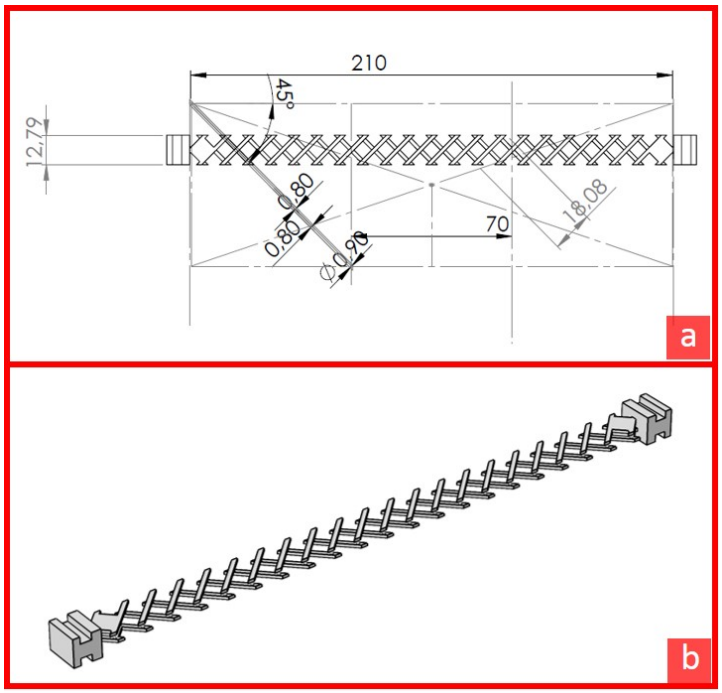

Fig. 2: Design of a pantographic beam with all the involved geometrical parameters. The dimensions are in mm.

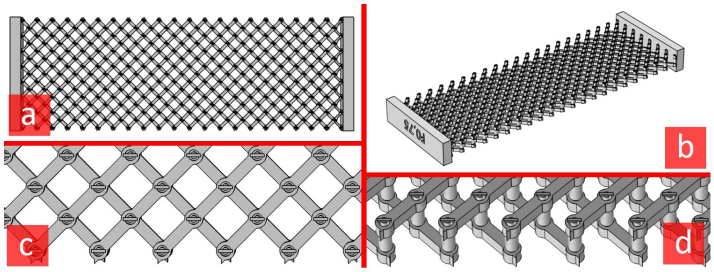

Fig. 3: Design of a pantographic structure with perfect pivots. The stl file can be both used for numerical simulations and for the manufacturing of a specimen.

were perfect hinges. The reason is related to technical challenges associated with the fabrication of perfect hinges. Additional details about this topic will be given in the following.

Figure 4, shows the design of a "millimetric" pantographic sub-structure, whose dimensions are approximately 1 cm $\times$ 3 cm. The fabrication of such a sub-structure, composed of a few basic units,allows for the analysis with

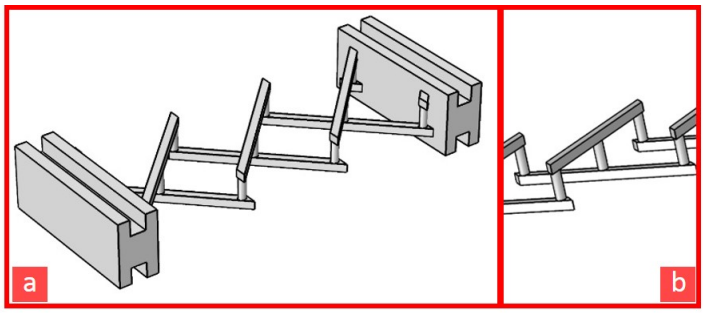

Fig. 4: CAD model of a so-called “millimetric” pantographic structure.

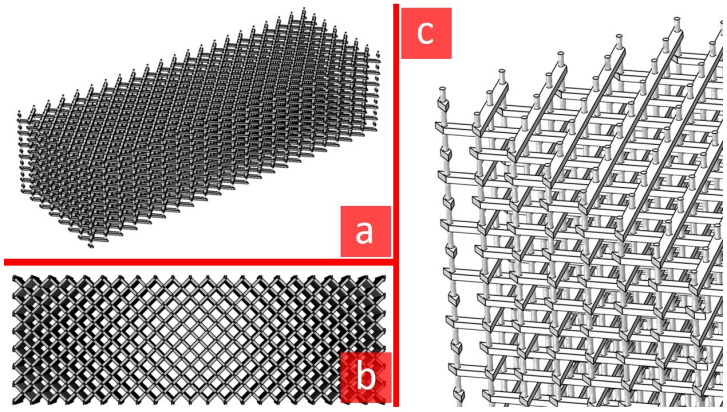

Fig. 5: Multi-layered pantographic structure.

greater details of the local behaviour of more complex structures made up of a larger numbers of primitive cells. A last example is reported in Fig. 5. This kind of pantographic structure is not a sheet-like material as those that have been presented so far. Instead, it is made up of many layers so that its depth cannot be neglected. With this design choice it is possible to supress the undesirable out-of-plane motions when performing some mechanical tests to determine in-plane deformability properties (*e.g.* three point bending test).

2.2 Additive Manufacturing

Recent advances in the technical capability of production and designing processes enables for the fabrication of materials having specific microstructures at small length scales, which have the ability to strongly condition the macroscopic mechanical response of the material. The fabrication of the pantographic structure considered herein, and other complex geometries, can now be per-

formed using "*3D printing*", also referred to as Additive Manufacturing (AM). For example, Selective Laser Sinterting (SLS) has already been employed for the production of lattice structures [21,22]). 3D printing is used to create objects with complex shapes in layer-by-layer procedures utilizing some precursor constitutive material. Most 3D printing processes employ wires or powders mainly made up of metallic or polymeric materials, which assume the designed shape by interacting with an energy source. For fabrication with 3D printing, the object must be designed and its three-dimensional geometry generated using a CAD software. The geometry is then discretized into a triangular/tetrahedral mesh and saved in the form of stl files. Such a file is then used as input for an AM software where the 3D geometry is sliced into layers, whose thickness can be set according to the needed resolution and machine capabilities, and the object to be made is positioned on the building platform. Before the printing process can start, it is necessary to design the supports that connect the object to the building platform and take on the functions of (i) supporting the part during the printing process, (ii) dissipating heat, (iii) avoiding thermal distortion. The particular case of metal additive manufacturing requires specific care to the minimization of overhanging areas where overheating zones usually are located and provoke a deterioration of the surface roughness.

The so-called powder bed processes are certainly the most promising among the AM techniques [23,24]. This category includes Selective Laser Melting (SLM), also called Laser Beam Melting (LBM), and Electron Beam Melting (EBM). The production process employs a laser (or electron) beam to melt a thin layer of powder. A resolution can be defined for such a process based on the size of the laser beam, being usually in the range between 50 and 100 μm, and the height of the powder layer in the range from 20 to 50 μm. Generally, the overlapping of hundreds of welding beds (200-300 μm in width) is needed to build a part (about 500 m of bead/cm^3 [25]), and the melting process is performed under shielding inert gas in order to prevent the oxidation of the powder. The shapes that can be built are complex and the objects, typically, have a satisfactory mechanical behavior [26].

2.2.1 Manufacturing of steel pantographic structures

In this survey, the SLM125HL set-up from SLM solutions has been used to create the pantographic structures. This machine is equipped with a 400W YAG laser (YLR-400-WC) at a wavelength of 1070 nm. The scanning speed varies from 400 to 1500 mm/s, while the thickness of the powder layer lies in the range between 30 and 100 μm. The minimum diameter of the laser at the focal point is about 70 μm. The powder employed is 316L stainless steel having spherical particles whose lowest diameter is 37 μm (CILAS 920). As mentioned above, the manufacturing of the part is preceded by the proper positioning of the 3D geometry in the printing volume using the MAGICS-Materialize Software. As depicted in Fig. 6, the specimens were positioned orthogonally to the building platform even though a tilt angle of 45^o would

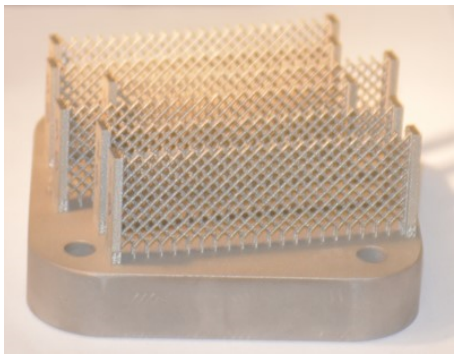

Fig. 6: Manufactured steel 316L samples.

have been preferable for the realization of the pivots. Despite the significant technological achievements represented by such manufacturing technologies, the objects obtained are very sensitive to the location and the number of supports whose inadequate positioning could result in widespread microstructural flaws. Furthermore, the rough surfaces in Figs. 7a,b show porosity which can potentially be suppressed by heat treatments such as Hot Isostatic Pressing (HIP), resulting in almost-fully dense metallic alloys [26] (such post processing was not performed on the samples presented in next sections).

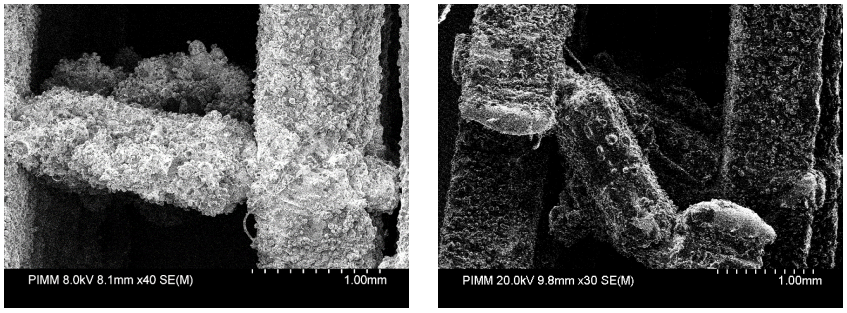

Fig. 7: SEM view of the beam pivot connection after tensile testing of 316L pantographic structure.

2.2.2 Manufacturing of aluminum pantographic structures

The following investigations were conducted with a commercial LBM system (EOS M 400), equipped with a $1kW$ laser unit (YLR-series, CW-laser, wavelength $1070nm$). All objects were manufactured with AlSi10Mg alloy (PSD: D10: $12.28\mu m$; D90: $43.22\mu m$) processed in $90\mu m$ layers under the influence of a heated building platform (165^oC). A shielding gas flow was applied parallel

to the top layer of the powder bed to remove any side products arising from the welding process.

General exposure strategy The process control and resulting material characteristics are intricate due to the incremental fabrication. An exposure strategy (arrangement of laser tracks) is necessary to create a volume using a spot-like energy source such as a laser beam. The exposure strategy in combination with exposure parameters like laser power and exposure speed define the material microstructure and therefore its characteristics. Due to different thermal boundary conditions, a part is usually divided into areas of different parameter settings (see Fig. 8). Areas in the surrounding of low thermal conductivity (*e.g.* powder) require different parameter settings compared to areas with increased thermal conductivity (*e.g.* surrounding solid material) in order to create a material of high quality (regarding factors like porosity, homogeneity or microstructure).

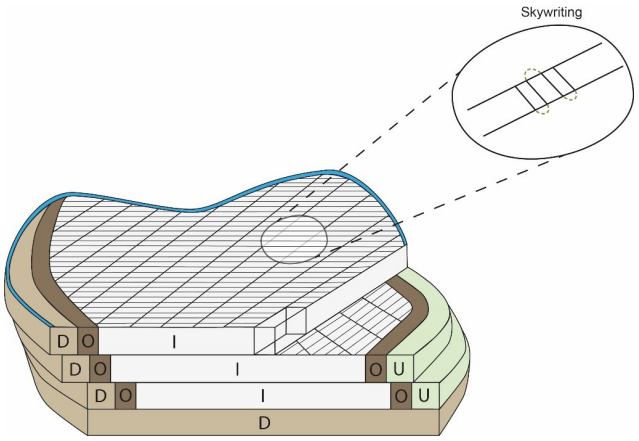

Fig. 8: Example of a basic exposure strategy (stripe strategy) and exposure areas. D: Downskin; U: Upskin; I: Inskin; O: Overlap; Blue: Contour exposure.

Laser track characteristics Usual exposure speeds for the processing of AlSi10Mg alloy can reach $2000 mm/s$. The switch on/off time of the laser unit can take up to $50 \mu s$. Therefore, the full laser power is reached after a distance of $\sim 0.1 mm$. This distance can also be impacted by delays in the electronics controls. This effect can cause different ending points for the laser track (see interrupt delays in Fig. 9). A second effect can be caused by the physical inertia of the projector mirror, which is resulting in a lower exposure speed in the beginning of the track, and therefore in a higher energy input.

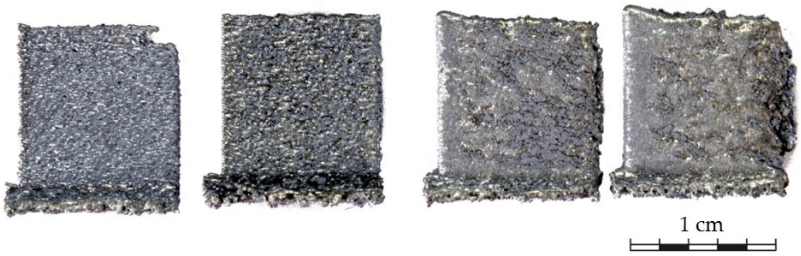

Fig. 9: AlSi10Mg alloy lamellas manufactured by a single laser track per layer, showing the impact of inertia (left sides) and interruption delay (right side). Left to right: increasing energy density.

Part orientation A proper orientation of a part within the building volume is essential to its quality and error-free reproducibility. Acute angles between the building substrate and the part's surface require a support structure. This is due to the residual stress within the material resulting from rapid cooling rates [27]. Without any connection of the part to the substrate, the former would deform within the process causing the coating unit to jam. Furthermore, surfaces with an acute angle result in poor surface quality regarding roughness, surface cracks and surface porosity. Therefore, it is advisable to avoid part orientations with major surfaces with acute angle.

Adapted manufacturing parameters for a metamaterial The AlSi10Mg alloy pantographic sheet was manufactured in a 45^o angle rotated about its axial direction in order to prevent any acute angle. All the surfaces show therefore a 45^o angle with respect to the substrate plate. A further advantage of this orientation is that the exposure cross-section within a layer offers more surface than the actual beam cross-section and therefore enables longer laser tracks. As a second measurement, a setup of a single exposure area was applied within the lattice. In order to increase the laser track length, circular laser tracks were applied instead of a stripe strategy. Furthermore, the exposure speed was minimized, which also required an adaption of laser power and hatch distance (spacing between laser tracks). As a result, it is possible to manufacture the pantographic sheet without any visual damage. A comparison of standard parameters and the adapted manufacturing parameters is illustrated in Fig. 10. The specimens were manufactured under the same building orientation.

Remark As mentioned above, parts produced by LBM exhibit increased residual stresses [28]. During the process, the support structures are counteracting to those forces preventing a deformation of the part. In order to prevent a deformation after the removal of the support structures, a heat treatment at 300 ^oC was applied for 2 hours. A comparison of the results is shown in Fig. 11, which shows the effect of heat-treatment on the final shape of the pantographic structures..

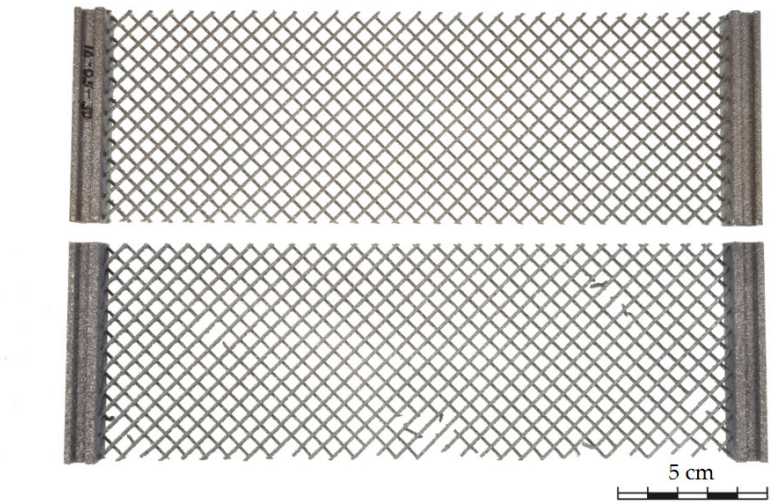

Fig. 10: Pantographic sheet with a beam diameter of 1 mm manufactured with AlSi10Mg alloy. Bottom: Sample manufactured by standard manufacturing parameters. Top: Sample manufactured by adapted exposure parameters and strategy.

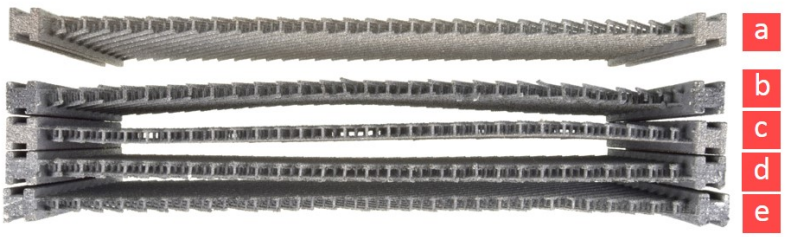

Fig. 11: Impact of heat treatment on global deformations of an aluminum alloy pantographic structures. (a) Heat treated pantographic sheet with no defects. (b) No heat treatment and manufacturing defects due to standard exposure strategy. (c) Heat treatment and manufacturing defects due to standard exposure strategy. (d)-(e) No heat treatment and no defect.

2.2.3 Fabrication of polyamide specimens

In case of polyamide samples, the chosen manufacturing technique is Selective Laser Sintering (SLS). In Fig. 12 a polyamide printed pantographic structure is shown. Many setting parameters are involved in the SLS (Selective Laser Sintering) 3D printing process, such as pre-heating temperature, laser power, bed cooling time [29]. A careful choice of the arrangement of prototypes in the virtual printing chamber is also required. A wrong orientation of the model,

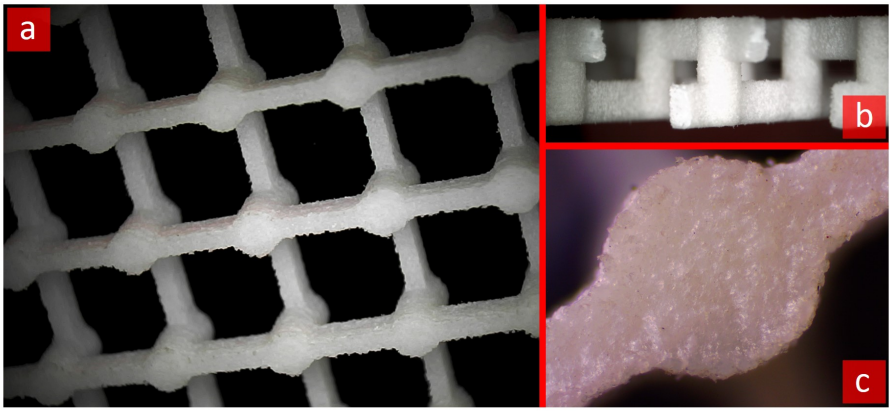

Fig. 12: Top view of the beam-pivot connection at the middle of the polyamide sample after tensile test (a). A detail showing the granulosity of the material (b).

especially when the model includes moving parts (as in the case of hinges in "perfect" pantographic fabrics), can affect their functionality or make a specimen completely useless [28]. After printing, especially in the SLS technology, it is necessary to wait until all the objects are cooled down in order to reduce material contractions. Wrong cooling procedures could lead to internal differential pre-stresses in the material, entailing impaired performances or even rupture of the printed specimen. In the end, the cleaning process is carried out. It is performed, for example, using air pressure, abrasive blasting or ultrasonic washers. A study is usually carried out in order to determine the optimal setting for specimens manufacturing and the optimal geometric properties of the CAD model [30].

2.3 Fabrication pantographic structures in microscale

As it has been shown in the previous subsections, advances in three-dimensional printing technologies have enabled the fabrication of arbitrary 3D metamaterial structures even at the microscale. Utilizing processes such as multi-photon lithography (MPL) and microstereolithography [31–33], the fabrication of pantographic structures in microscale has become feasible. In the present example, micrometric pantographic structures in 1 μm lengthscale have been fabricated and tested (the results of the tests are presented in the next section). The setup that was utilized is illustrated in Fig. 13. The apparatus has a FemtoFiber pro NIR laser with a wavelength of 780 nm, pulse width of 100 fs, and repetition rate of 80 MHz. The beam is focused by a 100× microscope objective lens (Plan-ApoChromat 100×/1.40 Oil M27, Zeiss). By tightly focusing the laser in the photosensitive material, the material was locally polymerized. The

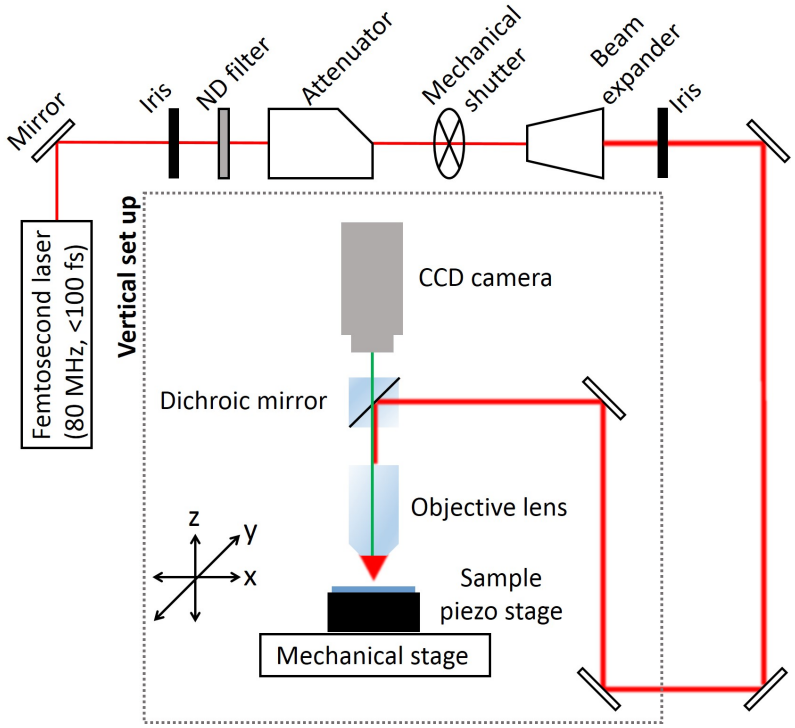

Fig. 13: Schematic of the MPL experimental setup [34].

stages were then translated so that the focused beam could "fabricate" inside the material and fabricate the three-dimensional structure of interest. In this fabrication method, the beams of the structure were designed as lines in the three-dimensional space. The geometry was then converted to a g-code, whose coordinates defined the geometry of the structure to be fabricated. Further information about the experimental setup can be found elsewhere [35]. The design of fabricated pantographic structures is presented in Fig. 14, imaged utilizing scanning electron microscopy. It should be noted that MPL is presently the only method capable of fabricating such complex 3D structures, as it is free of the intrinsic constraints of layer-by-layer printing techniques, architected the structure in a three-dimensional manner.

2.4 Fabrication of fiber-reinforced structures exhibiting pantographic-like responses

To demonstrate the industrial relevance of pantographic structures, experimental investigations have been conducted on thermoplastic composite lami-

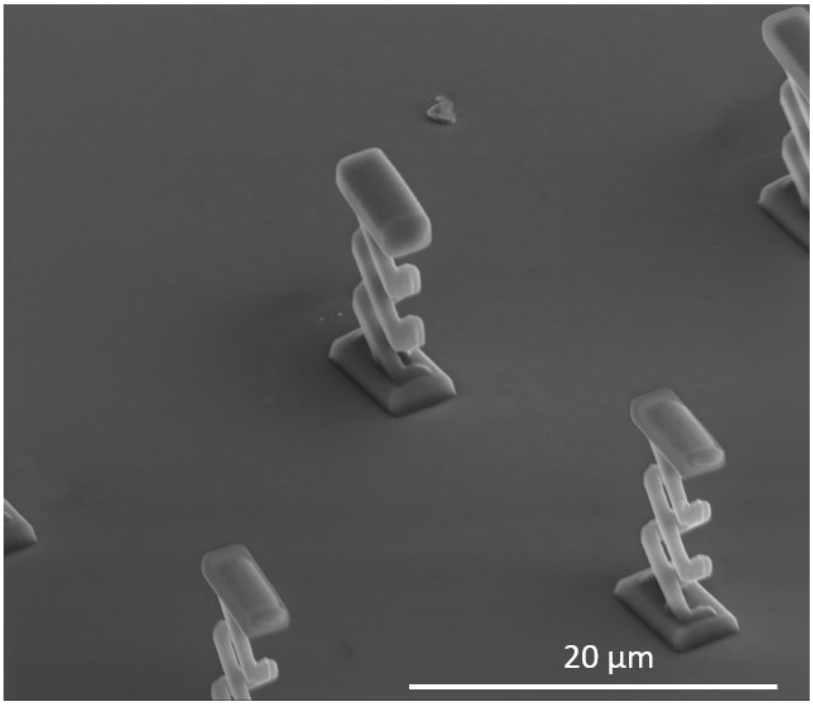

Fig. 14: Micro-pantograph image obtained by scanning electron microscopy.

nates, also known under the term *organic sheets* [36]. In particular, Tepexdynalite 102-RG600(1)/47 from LANXESS has been considered here as a prototypical example. This material consists of 47% vol. of a woven fabric (roving glass) and polycaprolactam (PA 6) as matrix material. The matrix material is hydrophilic with a maximum absorption of moisture between 2.6% and 3.4%. Notably, the used fiber-based prepregs are semi-finished products, which allows for a dedicated separation between production of prepregs and production of the final parts by forming. The forming temperature to be used within the forming process is between 240°C and 260°C, about 20°C above the melting temperature.

In industrial application, several layers with different fiber orientations are fused during the production. To obtain a clear view on the mechanical properties, a single layer material with a layer thickness of 0.5 mm has been made available by LANXESS. As can be seen in Fig. 15, the fibers are oriented similarly to the pantographic structure presented in Fig. 1. Moreover, Fig. 15 shows the differences between the warp and weft directions arranged as twill weave, leading to a slight unsymmetric mechanical behavior.

The surrounding matrix material stiffens the woven fabric and connects the junctions of the fibers in a similar manner as the hinges do for the pantographic structure. Consequently, this class of material consists of a homogeneous ma-

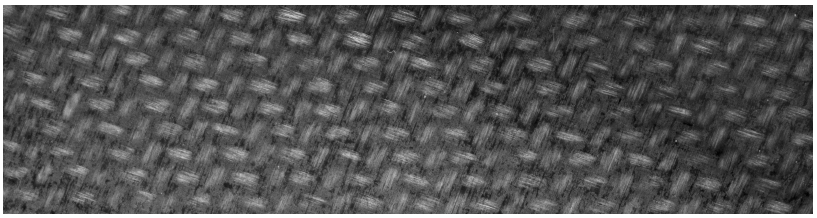

Fig. 15: Tepexdynalite 102-RG600(1)/47 organic sheet with pantographic-like structure, undeformed configuration.

trix with microstructures analogue to the pantographic structure with standard pivots, i.e. it acts like a combined first and second gradient material. It is important to note that additional stiffening mechanisms are present depending on the actual weave of the woven fabric, since stretching the fibers can lead to an increase of the stresses between the fibers at the junctions. This leads to complex reactions of the material especially in the inelastic regime. However, these effects cannot be separated within the experimental investigations, i.e. we always obtain a mean value of the material characteristics.

3 From experiments to modeling

In Ref. [14], a wide variety of models describing pantographic structures has been introduced. In particular, the Hencky-ty pe discrete model and the second gradient homogenized continuum model have been presented. In this section, different experimental tests validate those models. Moreover, new kind of measurements have been performed, needing sometimes the introduction of other types of kinematic variables.

In the subsequent discussion, results in different experiments, both static and dynamic, involving pantographic structures and pantographic-like (or pantographic-ispired) composite materials will be presented:

i. BIAS extension and shear tests of 316L steel specimens with standard and/or quasi-perfect pivots;
ii. BIAS extension of millimetric pantographic structures;
iii. BIAS extension of micrometric pantographic structures;
iv. torsion of aluminum alloy specimens;
v. BIAS extension of wide-knit polyamide specimens;
vi. dynamics polyamide pantographic structures with perfect pivots;
vii. extension test of a pantographic-like fiber reinforced composite;
viii. wrinkling in engineering fabrics.

Some of these experiments can be analyzed by using the models presented in Ref. [14]. In those cases where a different theoretical description is needed, elements of the newly developed models are given. First optimisation results have been obtained for structures subjected to tests as in (i).

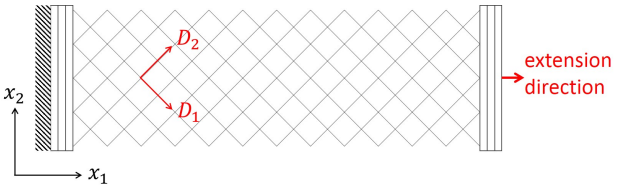

Fig. 16: Schematic description of a BIAS etension test.

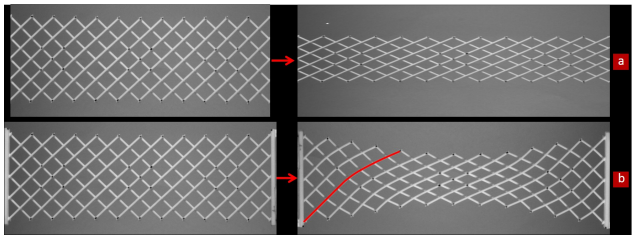

Fig. 17: (a) A pantograhic strucutre with no clamping deforms as a truss; (b) when the short sides are clamped, the bending of the fibers is observed.

3.1 Extension and Shear Tests of Steel Pantographic Structures

3.1.1 BIAS extension tests

The simplest experimental test one can perform on pantographic structures is known as BIAS extension test [19,37] (it is specifically called BIAS extension and not only extension, because it is performed along a biased direction respect to the fiber direction, see Fig. 16). This particular test is performed by clamping the short sides of the pantographic structure in order to observe the second gradient effects. In fact, as it is shown in Fig. 17, if the short sides are not clamped, then, in theory, one should measure zero deformation energy, because of the truss effect: up to the point when all the fibers become parallel the extension energy is zero (or negligible). By not clamping the short sides, the bending (second gradient) energy will also cancel out. Therefore this test has been conceived specifically to observe the second gradient effect.

When one wants to validate theoretically predicted phenomena, the possibility to really fabricate it has to be taken into account. In Fig. 3 the CAD model of a pantographic structure with perfect pivots has been shown. Depending on the dimensions (and possibly on the material) one decides to choose the printing process in order to obtain a real structure that will correspond more or less to the designed model. In particular, in Fig. 18 a comparison between the force-displacement plots of a structure with perfect pivots and with standard ones is shown. Both specimens are printed steel pantographic strucutres. If the

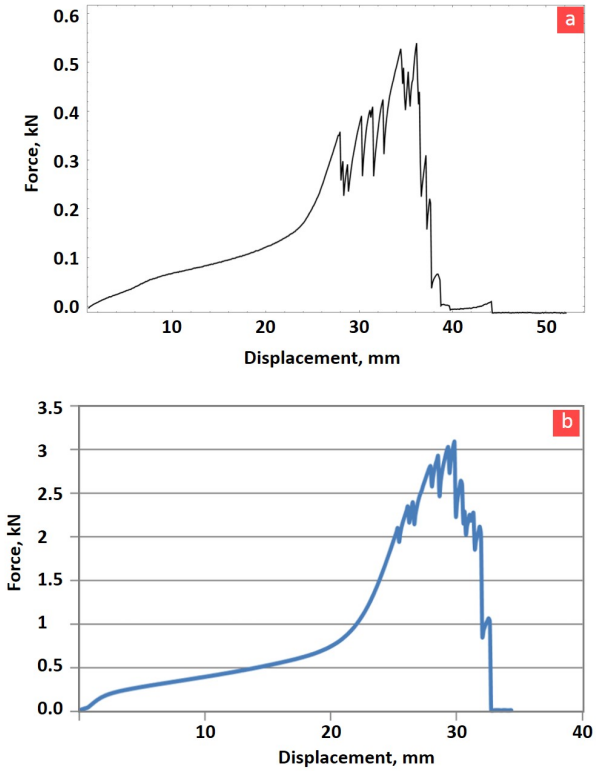

Fig. 18: Plot of axial force vs imposed displacement for a BIAS extension test performed on a 316L steel printed pantographic structure with (a) quasi-perfect pivots and (b) standard pivots.

model developed for pantographic structures is correct, then the total energy (and the force) related to the deformation should be composed of only the second gradient bending component, which is very low (some tens of N). By only observing the plot for the perfect-pivot specimen, it would seem that they have not worked in the right way. In fact, the measured force reaches some hundred of N. By comparing to the other case, the total force applied to the side of the structure is five times lower than the one when the pivots are in a standard configuration, carrying down their deformation (torsion) energy. It is possible to conclude that the perfect pivots were not completely well working, but, as it can be understood from Fig. 19, at the scale at which the pantographic structure was printed, it was not possible to obtain a very precise resolution. This leads to some friction between the internal cylinder and the external ring composing the hinge. The measured force is due to this internal friction mechanism. This effect will be analyzed in detail in future works.

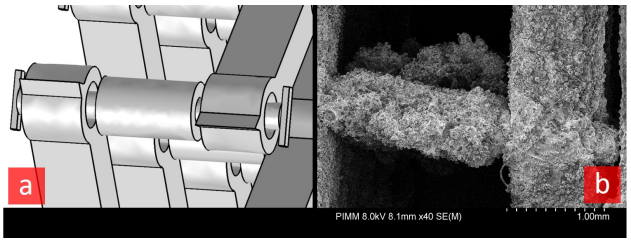

Fig. 19: CAD model of a perfect pivots (a) and its practical realization in 316L steel (b).

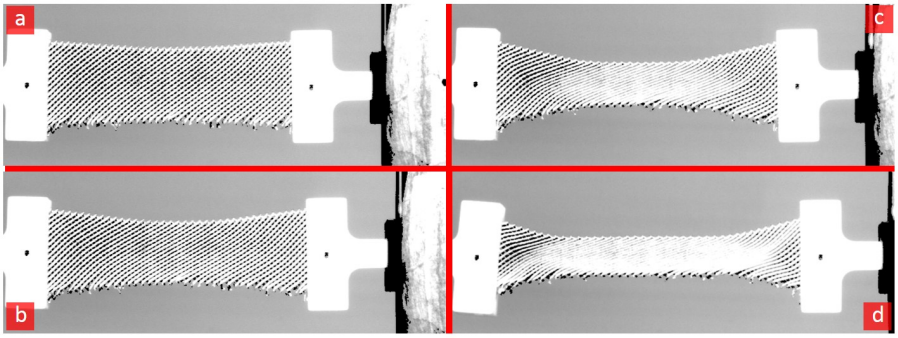

Fig. 20: Deformed shapes of a 316L steel pantographic structure.

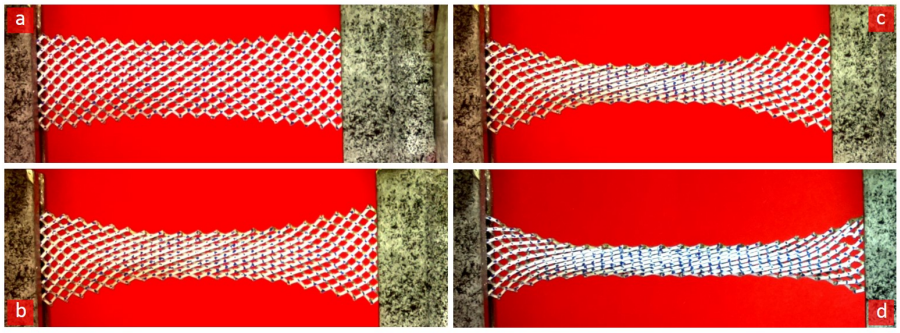

Fig. 21: Deformed shapes of a 316L steel pantographic structure with perfect pivots.

Damage-tolerance of pantographic structures The measured behavior under BIAS experiments also shows that the damage tolerance of pantographic structures is noteworthy. This aspect is understood from the force-displacement plots of Fig. 18 as well as that shown in Fig. 22 (the figures refer to a 3D printed specimen in stainless steel, with quasi-perfect pivots). The force-displacement diagram for pantographic fabrics customarily exhibits a peak at the end of

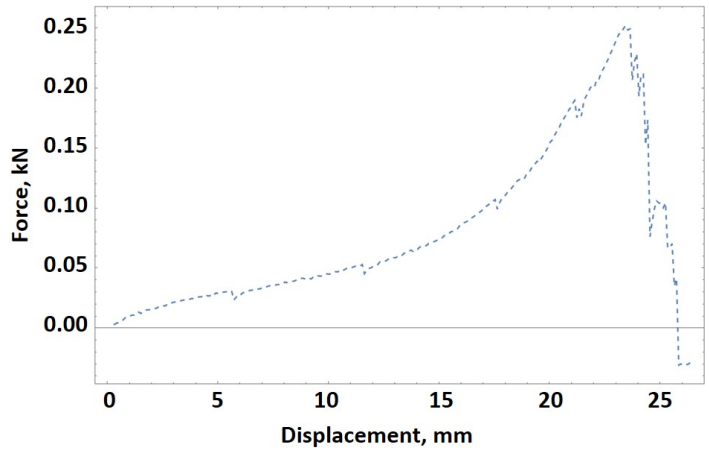

Fig. 22: Force vs displacement diagram for a pantographic structure with quasi-perfect pivots. In this test, the structure has undergone the subsequent rupture of several pivots. The main rupture events are noticeable by looking at small spikes before irreversible collapse of the structure.

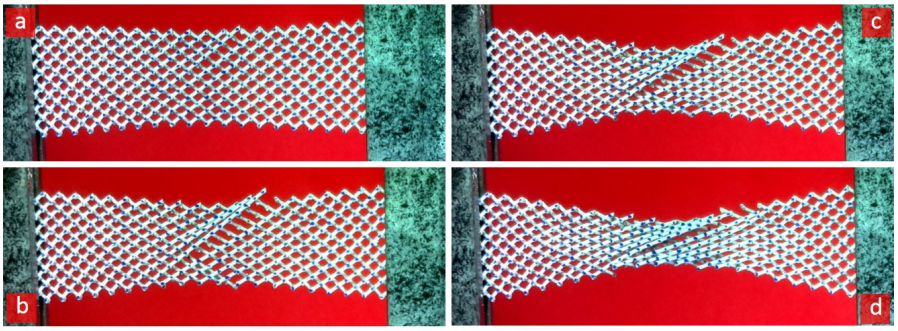

Fig. 23: Deformed shapes of a 316L steel pantographic structure with quasi-perfect pivots. Rupture of several pivots.

the stiffening stage. After the peak, the structure undergoes sequential rupture of its sub-components, typically the shearing of pivots, resulting in an avalanche-like softening.

The gradual softening leading to failure suggests that the topology of the structure and the deformability properties of its members are such that, when a sub-component rupture occurs, the load can be redistributed in a mitigating manner that prevents simultaneous catastrophic failure. In fact such damage-tolerance is also exhibited by the pantographic structure when failure of its sub-components occurs before the peak load (Fig. 22). Similar observations

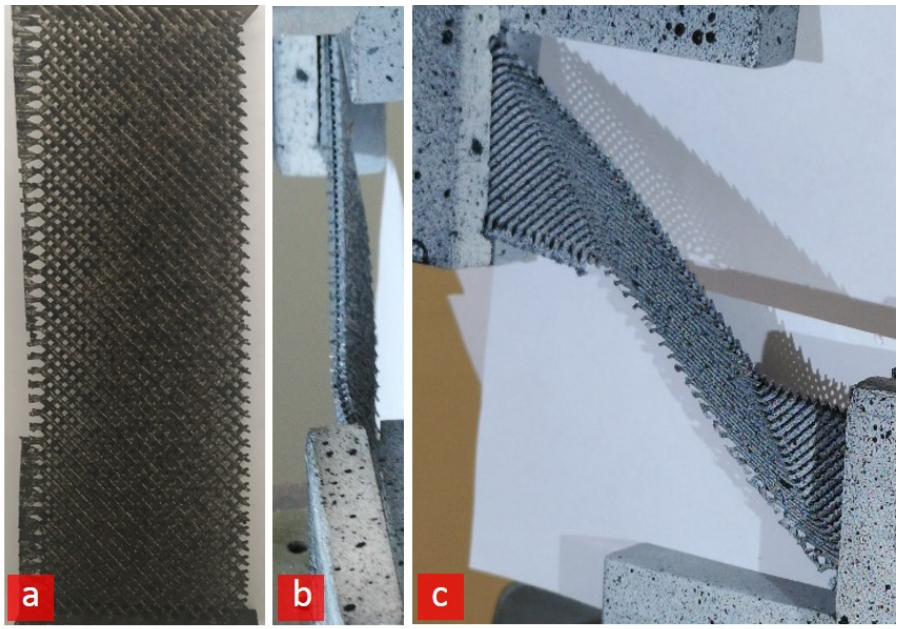

Fig. 24: A 316L steel pantographic structure with standard pivots in its reference configuration (a) and a step of deformation (b-c), where the out-of-plane deformation is evident.

across several specimens demonstrate the damage-tolerance of pantographic structures.

3.1.2 Shear tests

Another standard experiment to measure properties of pantographic structures is the shear test [38,39]. Some images of a shear test performed on a specimen with quasi-perfect pivots are shown in Fig. 25. This same test will be used in the following to show how the techniques developed in Digital Image Correlation can be suitably applied to pantographic structures. In particular, it has to be noted how by substituting standard pivots in the pantographic structure with quasi-perfect pivots, the whole structure gains in planar stability. Along a shear test the specimen exhibits buckling or wrinkling modes [40]. This phenomenon is related to the fact that there is the possibility that a buckled shape could have a lower energy with respect to an in-plane sheared shape. In Fig. 24 a steel printed specimen with standard pivots is shown. During the shear test a buckling mode occurred. If one compares the case of Fig. 24 to that of Fig. 25 (quasi-perfect pivots and no buckling), it is concluded that the lowered shear energy of the structure allows for plane deformations producing a pantographic structure which gains in planar stability.

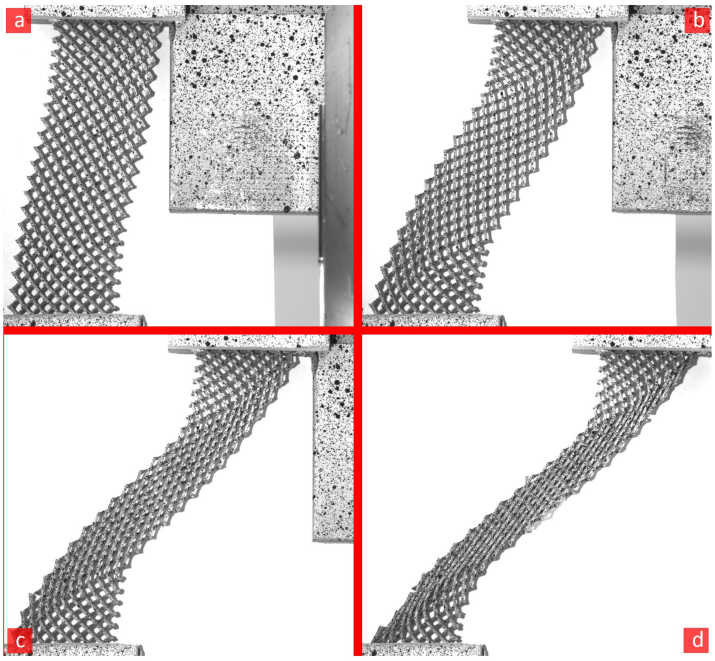

Fig. 25: Deformed shapes of a 316L steel pantographic structure.

3.1.3 Numerical simulations

Using a homogenized continuum model [15], it is possible to perform numerical simulations predicting the behavior under some experimental tests of such pantographic structures. In Fig. 26, the deformed shapes of the same specimen with quasi-perfect pivots analyzed previously (see Fig. 21) are compared to numerical simulations obtained for the same values of prescribed displacement. It is worth noting that, despite the simulations shown in Fig. 26 seem to be performed on a fibrous shape, the procedure to obtain them consists in the minimization of the energy associated to the pantographic structure [15] on a rectangular shape with the same dimensions as the real specimen. The contours on the right side of Fig. 26 are material lines corresponding to the real fibers of the specimen. In such a way, some parts of the rectangular continuum are "hidden" for only showing the material lines. This kind of numerical simulations will be compared in the following to simulations obtained by using a different model to describe pantographic structures, the so-called Euler-Bernoulli nonlinear beam based model [41].

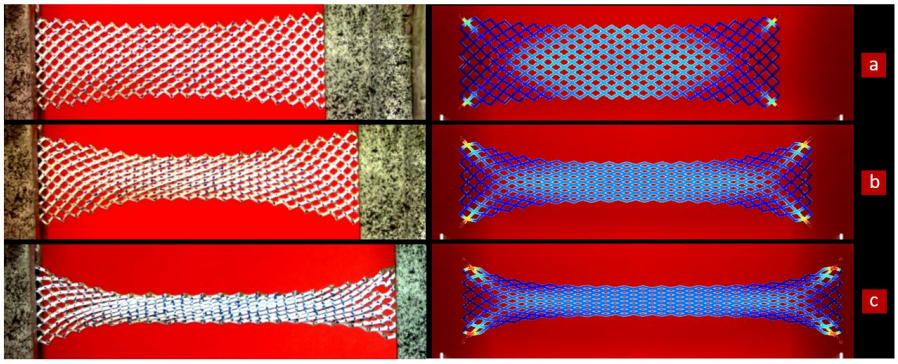

Fig. 26: Deformed shapes of a 316L steel pantographic structure.

3.2 Optimization in pantographic structures

As discussed in the previous section about experimental measurements, the problem of failure in pantographic structures is of primary importance. In Ref. [14], different descriptions and models of damage and failure in pantographic structures are exploited. On the one hand, it has been noticed that, for structures with standard pivots, the first rupture is located in one of the corners of the pantographic sheet. In Ref. [42] it has been shown how this kind of rupture can be modeled by considering the elongation of fibers. The fiber that is mostly elongated is the one at the corner of the rectangular sheet (see Fig. 27a). On the other hand, it has been observed how, when the aspect ratio of the pivots is very small (i.e. with high value of height over diameter ratio of pivots), the first rupture occurs no longer on some of the fibers but on the pivot itself, situated on the long side of the pantographic structure at $2/3$ of its length (see Fig. 27b). This mechanism has been analyzed in Ref. [43]. The aim of this section is to describe an optimization strategy for pantographic structures. The current development of the optimization procedure is based on the discrete Hencky-type model of pantographic structures [15, 42,14]. First results have been obtained in the case of constant short ratio pivots for which the prevalent rupture mechanism is based on the elongation of the fibers. The optimization methodology aims at maximizing the strength of the pantographic structure for which the failure mechanism is the breakage of beams in tension (see Fig. 28). The failure is in this case directly related to the axial strain energies of the beams. Because of the pantographic microstructure, any change of pivot diameter will not (as a first approximation) influence the bending and axial stiffness of the beams. It is then natural to look for an optimal spatial distribution of local shear pivot stiffnesses (varying from 0, *i.e.* perfect pivots, to infinity, i.e. clamped beams), which would lead to minimal axial deformation energy (see Fig. 29).

A fundamental point to be taken into account is that such an optimization problem must be constrained, otherwise the optimal distribution of pivot

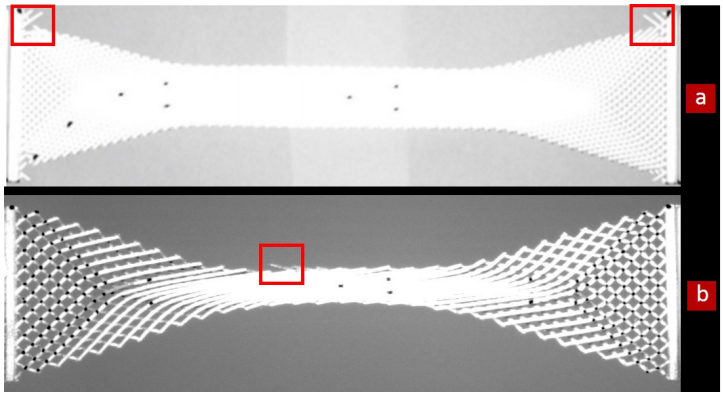

Fig. 27: Different typologies of rupture in pantographic structures. (a) A polyamide pantographic structures exhibiting the first rupture on the fiber of one of the corners. (b) An aluminum alloy pantographic structure in which the first rupture is observed on a pivot situated on the long side.

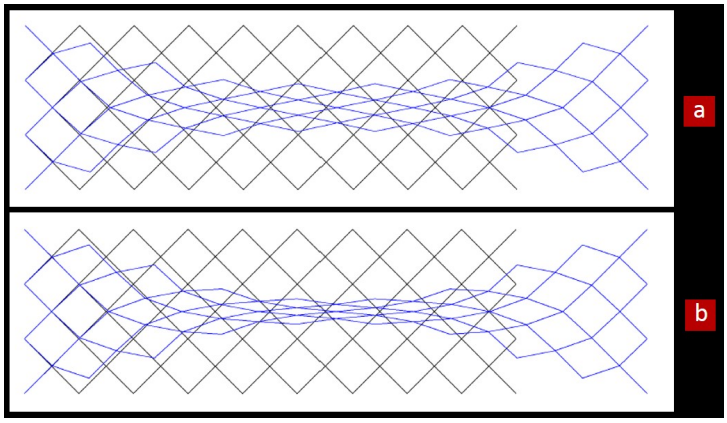

Fig. 28: Numerically computed deformed shapes of a pantographic structure with (a) constant stiffness for all the pivots and (b) optimized stiffnesses.

stiffnesses would cancel out shear stiffness everywhere, as it would result in a zero pantographic structural stiffness, in other words a mechanism, that would never break. A reasonable constraint is that the final structural stiffness remains unchanged, which allows for a different total deformation energy between initial and optimized structures. As experimental results with constant shear pivot stiffness are available [44], the previously described optimization methodology was performed numerically with such initial design. The optimal pantographic structures have yet to be constructed in order to validate the effective numerical increase of the strength of such structures.

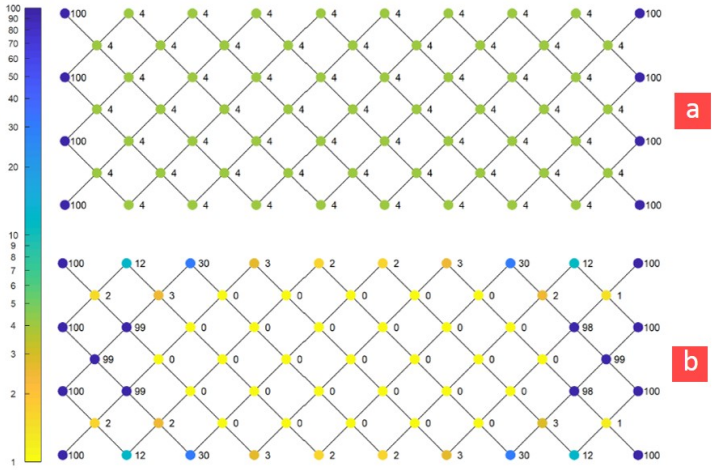

Fig. 29: Distribution of the stiffnesses of pivots in (a) "standard" pantographic structure and (b) optimized pantographic structure.

Future perspectives A first generalization of the above discussed optimization strategy is to consider axial, bending and shear stiffnesses simultaneously as distributed optimization parameters. A second generalization is to consider the case of small ratio pivot structures. In that case, the total energy of the pantographic structure has to be completed with an additional term depending on the relative displacement of the fibers of the two families in correspondence with the interconnecting pivot [43].

3.3 Millimetric pantographic structures

We refer in the sequel to specimen as shown in Fig. 4 as *millimetric pantographic structure*. In Fig. 30, selected experimental measurements on these types of specimen are compared with the theoretical predictions based upon the enhanced Piola–Hencky model [45]. By means of this model, it is possible to obtain good agreement with experimental data. In Fig. 31 the computed deformed shapes are compared to the measured ones.

3.4 Mechanical testing of pantographic structures in microscale

To examine the mechanical performance and compare it with the mathematical discrete model of Hencky-type [42], mechanical tests were performed with a nanoindentation apparatus (TI 950 TriboIndenter, Hysitron) which enables high-precision nanomechanical testing. In this study, only quasistatic indentation tests were conducted. For the metamaterial structures, the maximum

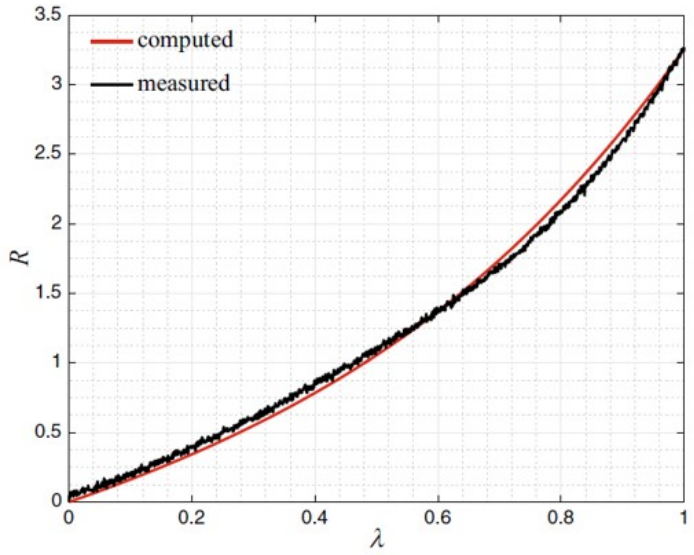

Fig. 30: Force-displacement diagram for a polyamide millimetric pantographic structure. Comparison between experimental data and predictions based on the enhanced Piola–Hencky model. The displacement is expressed in terms of the dimensionless ratio $\lambda = \frac{\Delta L}{L_0}$.

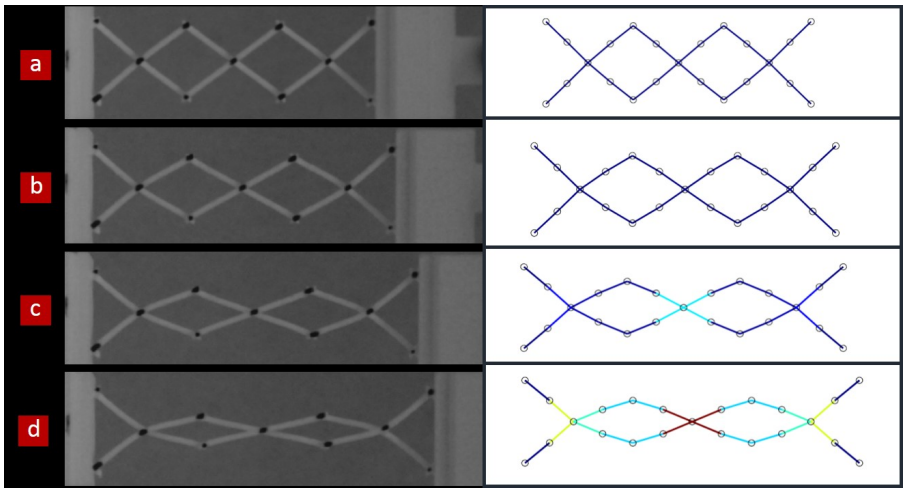

Fig. 31: Deformed shapes of a polyamide millimetric pantographic structure for different values of the prescribed displacement (left) and comparison with numerical simulations (rigth).

compressive distance was set at 2 μm. Typical indentation results for two specimens are shown in Fig. 32. Comparison of the experimental and simulation

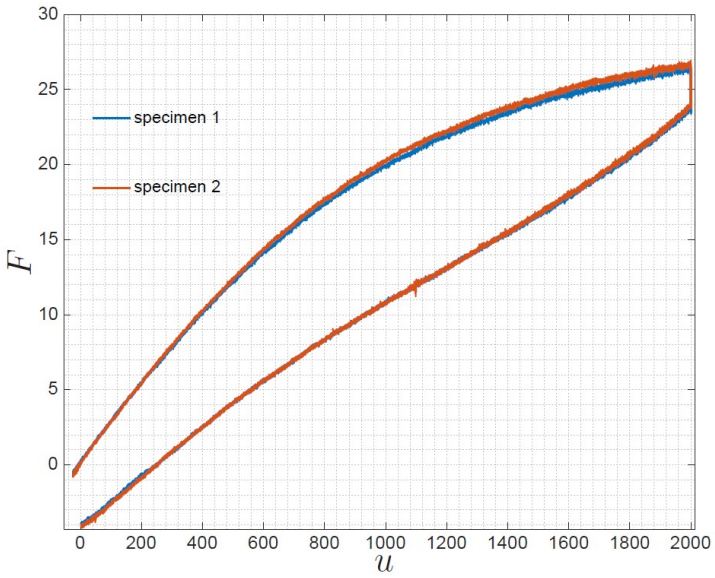

Fig. 32: Force F in the direction of the longer side of the pantograph, in μN, vs. displacement u, in nm, for the compression test: experimental results for a pair of identical specimens.

results is illustrated in Fig. 33. It must be remarked that both the experimental and numerical curves are aligned, at least until values of given displacement u less than 1500 nm proving the validity of the simple Hencky-type model. These findings elucidate that the fabrication and modelling of pantographic can facilitate the design of nonlinear 3D architectures in microscale for engineering applications. Nevertheless, mechanical tests in different deformation modes should be introduced, to advance the study of the mechanical behaviour for pantographic structures. We aim to conduct tensile experiments, utilizing the design of push to pull up mechanisms [46]. SEM micrographs of the architected design is presented in Fig. 34. Moreover, we will utilize in-situ scanning electron microscopy with microindentation to visualize the mechanical response of the material through the mechanical testing. As we will integrate the experimental measurements of the deformation patterns of micro-pantographs with the experimental results with the available numerical simulations, we will pave the way to assemble the field of theoretical mechanics with the design and fabrication of metamaterial structures in microscale for a plethora of applications, such as shape memory alloys actuation [47] and scaffolds for tissue engineering [48].

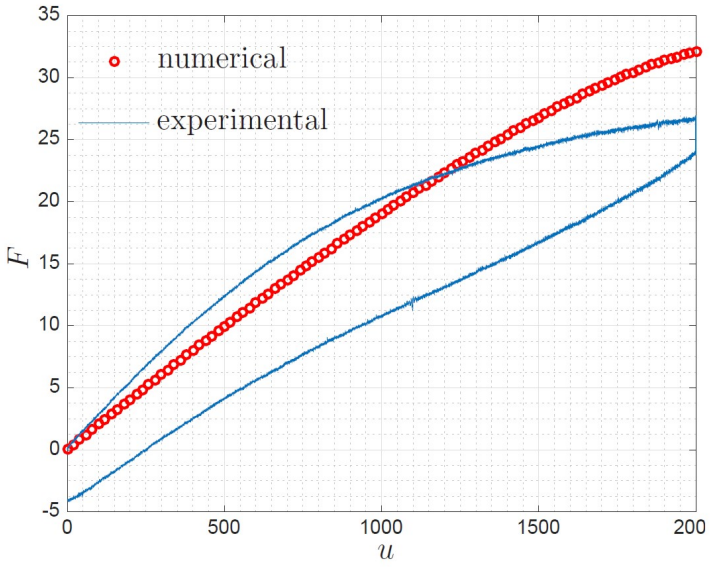

Fig. 33: Force F in the direction of the longer side of the pantograph, in μN, vs. displacement u, in nm, for the compression test: numerical (in red) and experimental (in blue) results.

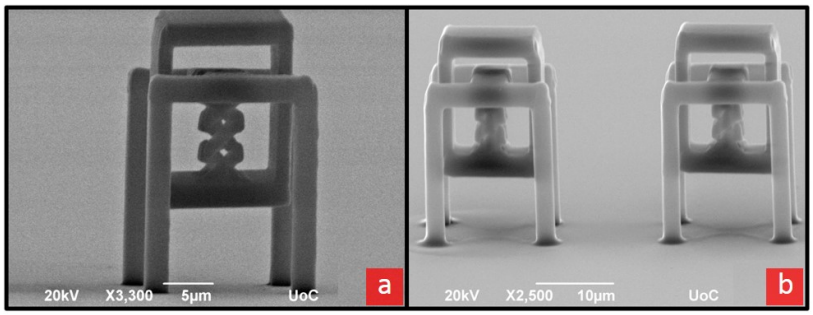

Fig. 34: Push to pull up mechanisms for pantographic structures fabricated with MPL. This design has been used to conduct tensile mechanical tests to study the mechanical behaviour of the micro-pantographs and juxtapose it with the theoretical modelling.

3.5 Wide-knit pantographic structures

When pantographic structures are constituted by just few fibers (see Fig. 35) they cannot be properly considered fabrics. In this case they are referred as wide-knit pantographic structures and the constituting fibers can be modeled

as Euler-Bernoulli beams. This model has been numerically implemented by using (i) isogeometric analysis in [49,50] and (ii) a Ritz approach in [41]. If,

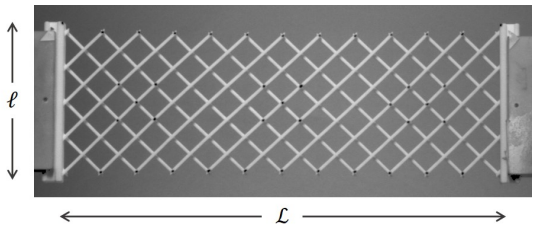

Fig. 35: Example of wide-knit pantographic structure.

instead, the lattice is dense, as it has been already clarified, a homogenization procedure leads to a two-dimensional second-order gradient continuum model.

3.5.1 Isogeometic analysis method

A rotation-free discretization is obtained with isogeometric analyses [49,50] that provide basis functions with a higher inter-element continuity. We consider a lattice composed of two uniform orthogonal families of beams having for main directions x and y (Fig. 36). All the aligned segments form a single continuous beam and two consecutive parallel beams are separated by the distance e. The pivots linking the displacements between two intersecting beams are described in Ref. [15] and are enforced by Lagrange multipliers ($\boldsymbol{\lambda}^{(ij)} \in \mathbb{R}^2$).

Fig. 36: Pantographic lattice of ratio 3 : 1 and composed by 78 beams ($e = 4.8$ mm).

Discrete and continuum models Using a rotation-free geometrically nonlinear Euler-Bernoulli beam formulation, the deformation energy of the discrete

photographic lattice is given by

$$W_{Latt} = \sum_{s=\{x,y\}} \sum_{n} \int \left(\frac{EA}{2} \left(\epsilon^{(n)}_{\{,s\}} \right)^2 + \frac{EI}{2} \left(\kappa^{(n)}_{\{,s\}} \right)^2 \right) ds + \sum_i \sum_j \frac{k_\theta}{2} \left| \sin^{-1} \left(\overline{\boldsymbol{r}_{,y}}^{(i)} \cdot \overline{\boldsymbol{r}_{,x}}^{(j)} \right) \right|^\gamma + \left(\boldsymbol{r}^{(i)} - \boldsymbol{r}^{(j)} \right) \cdot \boldsymbol{\lambda}^{(ij)}, \quad (1)$$

where $n = \{j, i\}$ for $s = \{x, y\}$, respectively, E Young modulus, A the cross section area, I the area moment of inertia, k_θ and γ are two parameters that characterize the pivots. $\epsilon_{\{,x\}}$ and $\kappa_{\{,x\}}$ are the membrane and bending strains, respectively [49].

Assuming a small distance e between the beams, the sums of Eq. (1) can be replaced by integrals, leading to an homogenized media [15]:

$$W_{Cont} = \int \int \left(\sum_{s=\{x,y\}} \left(\frac{K_\epsilon}{2} \left(\epsilon_{\{,s\}} \right)^2 + \frac{K_\kappa}{2} \left(\kappa_{\{,s\}} \right)^2 \right) + \frac{K_\theta}{2} \left| \sin^{-1} \left(\overline{\boldsymbol{r}_{,y}} \cdot \overline{\boldsymbol{r}_{,x}} \right) \right|^\gamma \right) dxdy, \quad (2)$$

where $K_\epsilon = EA/e$, $K_\kappa = EI/e$ and $K_\theta = k_\theta/e^2$.

In both expressions, the bending strain is also called the curvature, and depends on the second derivative of the displacement field, thereby requiring at least C^1-continuous shape functions.

Isogeometric analysis Introduced by Hughes et al. [51], the isogeometric analysis consists in reusing the shape functions that describe the geometry for the analysis. These shape functions are most often non-uniform rational B-splines (NURBS) and represent exactly conic shapes. One of the main advantages of this method is that the inter-element continuity can be augmented through the k-refinement procedure. This property has been successfully adopted to solve rotation-free second-order weak formulations, as encountered for instance in structural mechanics for Kirchhoff–Love shells [52] and beams [53]. Isogeometric analysis has been successfully applied to elastic beams and Kirchhoff plates [54–61].

Numerical results The pantographic lattice investigated in Ref. [15, 49] is reproduced. Four different displacement conditions are applied (see Fig. 36, $\xi = BC/\|BC\|$, $\eta = BA/\|BA\|$)

- Test a: AB is motionless, CD is translated by the vector 0.0567ξ.
- Test b: AB is motionless, CD is translated by the vector $2H\eta$.
- Test c: AB is motionless, CD is translated by the vector $0.5H\xi$ and anticlockwise rotated by $\pi/4$ about its center.
- Test d: AB is clockwise rotated by $\pi/3$ about A, CD is rotated anticlockwise by $\pi/3$ about the point D and translated by the vector $-3/2H\xi$.

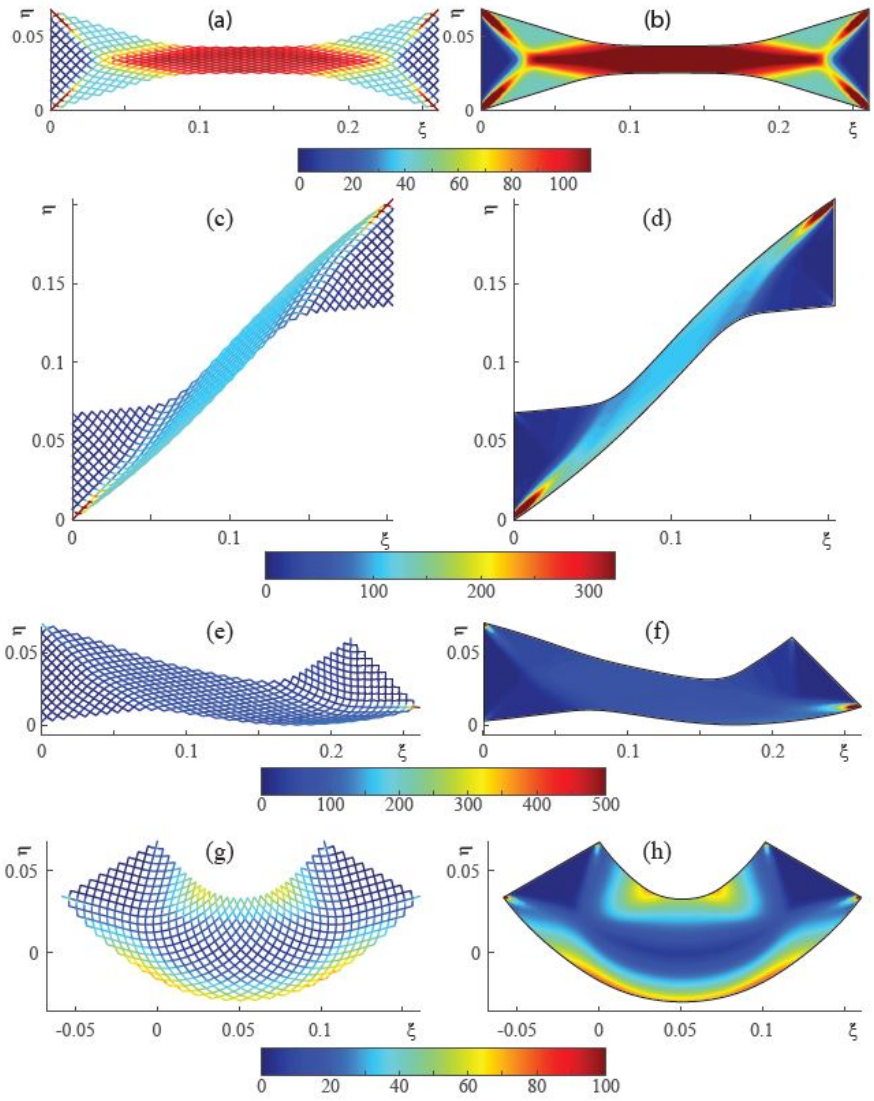

Fig. 37: Tests a (a,b) b (c,d) c (e,f) and d (g,h): total strain energies (J/m^2) predicted by discrete (a,c,d,f) and continuum (b,d,f,g) models.

The deformation energies for the four cases are shown in Fig. 37. The homogenized models are found to be in excellent agreement with the discrete version. In order to provide a more accurate comparison, the discrete model of case a is refined with different beam densities. The tension applied to the edge CD, the angle between the two fibers intersecting at the middle of the

Table 1: Test a:, applied tension, angle in the middle of the specimen, and elongation of the fiber indicated with an arrow in Fig. 36 for discrete lattices with different beam densities, and the isogeometric continuum model.

	Force (N)	Angle (°)	Elongation (%)
IGA lattice ($e = 9.6$ mm)	67.1	24.1	3.51
IGA lattice ($e = 4.8$ mm)	62.0	21.9	4.88
IGA lattice ($e = 2.4$ mm)	59.6	21.6	5.04
IGA lattice ($e = 1.2$ mm)	58.8	21.4	4.75
IGA continuum ($e = 0$)	58.6	21.2	4.66

specimen, and the elongation of the fiber indicated by an arrow in Fig. 36 are reported in Table 1. When the lattice density is increased, the discrete results converge to the continuum model.

3.5.2 Ritz approach

A second possibility to minimize the energy introduced in Eq. 1 consists in adopting a Ritz approach by distretizing the above mentioned energy and by introducing some shape functions to describe the displacements. A relevant difference between the energies considered in [41] and the one reported in Eq. 1 consists in the description of the pivot. For describing a real pantographic sheet, one is obliged to introduce an energetic term related to the torsion of the pivots (at the micro-level, while, at the macro-homogenized level, it has to be related to the shear in the pantographic sheet). This torsional term is present in both the descriptions. Following the ansatz presented in [43], in [41] it is considered an addtional term in order to take into account the possibility that fibers of different families slide one with respect to the other in correspondence of a pivot (which in a micro-description of the problem can be interpreted as the energy relative to the flexion or the shear of the pivot). Due to the order of the derivatives appearing in the nonlinear Euler-Bernoulli beam theory, the axial displacement u and transverse displacement v require, at least, functions with continuity C^2. Therefore, in the local reference system the generalized displacements (u, v) inside the element are interpolated from some (nodal) local displacements written in terms of the Hermite cubic polynomials.

After the minimization of the potential energy, the equilibrium shapes of the pantographic structure are obtained. A comparison between the experimental measures and the numerical computed deformed shapes is given in Fig. 38.

3.6 Torsion of pantographic structures

Due to their peculiar geometrical arrangement, pantographic structures show unusual responses in torsion. The mechanism that has been measured in torsion tests of aluminum alloy printed pantographic structures is known as the

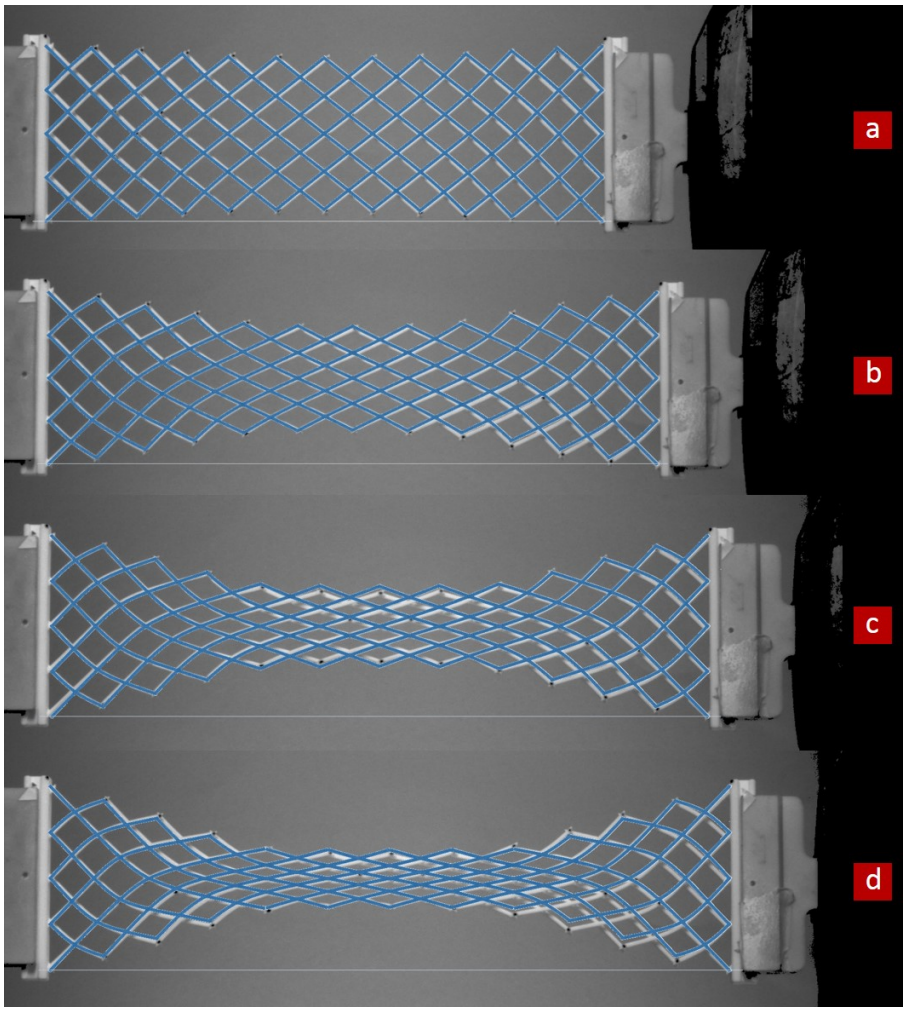

Fig. 38: Superposition of experimental (gray) and numerical (blue) shapes for four different values of the prescribed displacements in a BIAS extension test: (a) 0.014 m, (b) 0.037 m, (c) 0.048 m, (d) 0.054m

nonlinear Poynting effect [21]. The Poynting effect is observed in elastic materials, for example, during the torsion of a beam. It is considered as an axial effect. Also if there are no axial loads, due to torsion the length of the beam changes. Conversely, if the beam has motionless ends, an axial reaction force appears. This axial force has been measured during torsion tests. Its change with the torsion angle is represented in Fig. 39 (for the different tested specimens).

The different responses that are reported in Fig. 39 can be explained by considering two competing mechanisms, namely, the bending of the fibers and

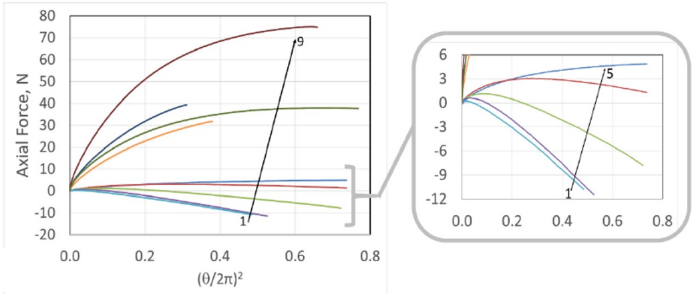

Fig. 39: Torsion tests results. Axial reaction force versus rotation angle. The usual Poynting effect would be represented by a linear trend.

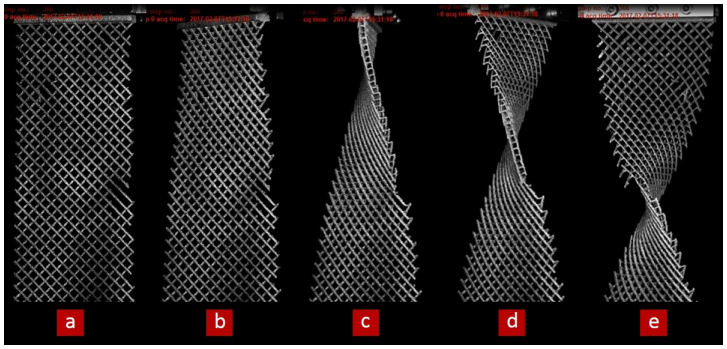

Fig. 40: Torsion of an aluminum alloy pantographic structure evidencing the Poynting effect reversal.

the shearing of the pivots. On the one hand, when the shearing of the pivots is more important than the bending of the fibers, the angles between the fibers change while the fibers keep their length, resulting in a reverse Poynting effect. On the other hand, if the bending of the fibers is predominant, then the whole structure will be stretched in the direction orthogonal to the twist axis, with a positive Poynting effect (Fig. 40). It has to be noted that the above considered phenomenon is a double-scale issue. This observation implies that it cannot be treated in the framework of the standard Cauchy Continuum Mechanics, but a generalised (in this case a second gradient) model has to be taken into account [62].

3.7 Dynamics of pantographic sheets

In this section, the experimental results on the dynamical behavior of a pantographic sheet [63] are briefly reviewed. In particular, a qualitative description of the dynamic displacement vector fields observed on a pantographic sheet

clamped at one end and undergoing a sinusoidal (uniaxial) imposed displacement at the other end is discussed. Moreover, the measurement process and the experimental setup will be described.

3.7.1 Experimental arrangement

The studied pantographic sheet is a 3D-printed polyamide EOS PA22000 rectangular (linear dimensions: 235 $\times$ 78 mm) specimen. The sample is prepared with a speckle pattern aimed for Digital Image Correlation analyses (see below). One of the short ends of the sample is clamped to the ground while the other one is connected to a Brüel & Kjær type 4809 shaker driven by a Brüel & Kjær type 2718 power amplifier (see Fig. 41). Before each measurement, preparatory checks on the position of the specimen with respect to the ground and to the shaker are performed. Measurement consists in a direct time observation by means of two Phantom v1612 cameras of the dynamic behavior of the sheet undergoing a sinusoidal displacement prescribed by the shaker. The acquisition rate is 2048 images/second with a definition of 1280 $\times$ 800 pixels [64]. Two Nikon 200 mm macro lenses are used for the cameras. For a distance of $\sim$1.5 m, the field of view of the cameras is $\sim$240 $\times$ 150 mm [65]. The sample is illuminated by means of four halogen spotlights (250 W each). The maximum theoretical resolving power for the 3D DIC depends on the proprietary software LaVision DaVis 8.3 used and in these conditions is $\sim$10 μm [66]. Stereovision calibration is performed by means of a pinhole camera model. In particular, to minimize mapping errors associated with sample volume, five different views of a two-level calibration plate are considered. The re-projection error is 0.13 pixel in RMS. All the displacements observed refer to a picture of the sample at rest, being the reference configuration for the different data sets. Finally, to avoid unwanted buckling phenomena during the measurement, the specimen is fixed in a pre-stressed configuration (237 mm vs 235 mm in the relaxed configuration).

Measurements are performed for 24 different frequencies, ranging from 30 Hz to 200 Hz with a step of 10 Hz. For each frequency, three increasing excitation amplitudes and both orientations are considered. Moreover, to try to limit any dependence of the measurement results on environmental conditions (such as heating of the specimen due to oscillations), the frequency range is spanned both increasing and decreasing the frequency levels. Setting one frequency, one orientation and one amplitude, the measurement is performed in the following way

1. From a National Instrument NI-9263 analog output module a monochromatic signal is generated and sent to the amplifier;
2. Given the elastic nature of the sample, it is assumed that after 2.5 s it reaches the steady state. A trigger signal is then sent from the output module to the cameras;
3. Both the excitation signal on the amplifier and the 500 video frames acquired by each camera are stored for the following data analysis.

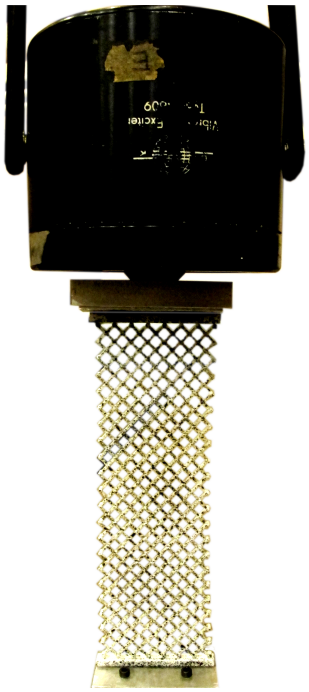

Fig. 41: Polyamide pantographic sheet connected to a shaker.

The algorithm to obtain the displacement vector fields is a least square match with a step size of 4 pixel and a 19 × 19 pixel window size.

3.7.2 Measurement results

According to the previously explained procedure, it is possible to observe the dynamic displacement vector field of a pantographic sheet clamped at one end and sinusoidally oscillating at the other end. In this section,the results for a set of relevant frequencies are presented.

In Figs. 42 - 44 it is possible to observe the displacement vector field at maximum displacement (oscillation peaks) for 30 Hz, 50 Hz (Fig. 42); 100 Hz, 120 Hz (Fig. 43); 140 Hz, 200 Hz (Fig. 44) frequencies. For each frequency, two snapshots corresponding to the maximum displacement are shown. The arrows depict the in-plane displacements while the colors represent the amplitude of the out-of-plane displacement.
The in-plane displacement vector fields appear curved. The position of curvature centers and the curvature itself appear to be dependent on the frequency. The rapid change in the displacement vector field when the frequency approaches 200 Hz suggests that it is close to resonance. The pantographic sheet rotates around its vertical middle axis resulting in out-of-plane displacements. The higher the frequency the lowest is the amplitude of out-of-plane displace-

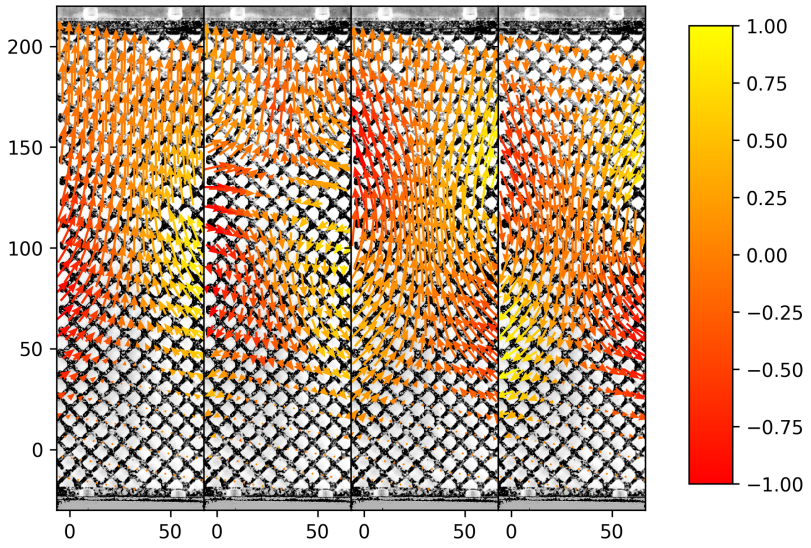

Fig. 42: The first two plots refer to an excitation frequency of 30 Hz while the other two refer to an excitation frequency of 50 Hz. The arrows depict the in-plane displacement while the color represents the amplitude of the out-of-plane displacement (all expressed in mm). The shaker is connected to the top end while the sample is clamped to the ground at the bottom end.

ments. In particular for the highest frequency its peak-to-peak amplitude is negligible, allowing for a forthcoming 2D modeling.

These results have to be considered as a starting point for both experimental and modeling efforts aimed at understanding the dynamic behavior of pantographic metamaterials. In particular, several interesting experimental variations of the methods presented in this section can be considered. As an example, one may be interested in the dynamic behavior of a damaged specimen or in larger deformations to observe nonlinear phenomena. From the modeling point of view, the possibility to have experimental benchmarks for the theoretical models will be exploited to make a selection process of the manifold of models and approaches in this very active framework.

3.8 Extension tests of pantographic-like fiber reinforced structures

For the subsequent tests on the fiber reinforced material, standard specimens of size 125×25 mm and 125×36 mm have been cut from a larger plate using a hydraulic shear. Additionally, to prevent slip between the universal testing machine and the specimen, large clamping forces are required. Therefore, additional 20 mm long cap strips (width is adjusted to the sample) made from the same material with fiber orientation rotated 45° against the orientation of the

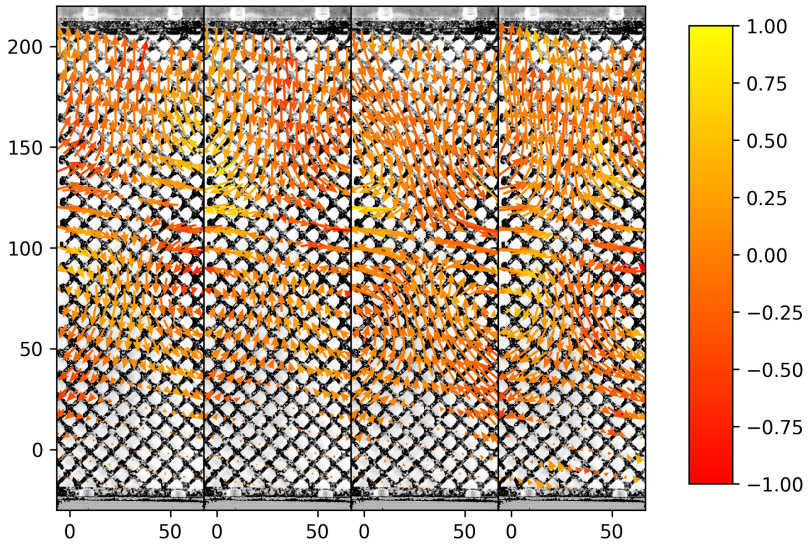

Fig. 43: The first two plots refer to an excitation frequency of 100 Hz while the other two refer to an excitation frequency of 120 Hz. The arrows represent the in-plane displacement while the color represents the amplitude of the out-of-plane displacement. The shaker is connected to the top end while the sample is clamped to the ground from the bottom end.

fibers of the samples have been glued both sides at the ends of the specimen. Figure 45 displays the clamping system for a 36 mm specimen.

First, a force-displacement diagram for the 25 mm specimen is shown in Fig. 46. Different orientations of the fibers have been investigated, namely, 0° (warp direction) and 90° (weft direction). For both directions, nearly identical results are observed. The junctions between the fibers are not active, i.e. the fiber-reinforced material acts like a first-gradient material and breakage occurs beyond 5 kN (not displayed in the diagram for the sake of clarity on the other measurements). For 15° and 75° directions, the results are again similar, with a slight increase of the stiffness for the 15° direction. The same increase in stiffness is observed between 30° and 60° directions. It is worth noting that the fluctuations within the measurements are small, as demonstrated in Fig. 47 for a series of measurements with the 75° fiber orientation.

The peak forces before fracture starts depend on the orientation of the fibers. As shown in Fig. 48, the fracture patterns are different. Similar to printed pantographic structures, the fiber reinforced laminate undergoes gradual damage after the peak. The fibers break in a cascading manner leading to the same type of load redistribution as observed before.

Perspective: modelling via mean Green operators homogenization procedure
An important subclass of composite materials is represented by "network-

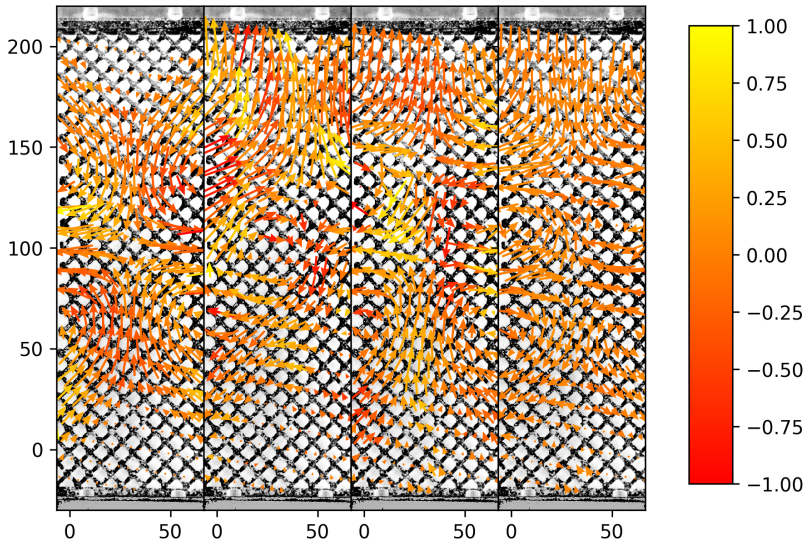

Fig. 44: The first two plots refer to an excitation frequency of 100 Hz while the other two refer to an excitation frequency of 120 Hz. The arrows represent the in-plane displacement while the color represents the amplitude of the out-of-plane displacement. The shaker is connected to the top end while the sample is clamped to the ground from the bottom end.

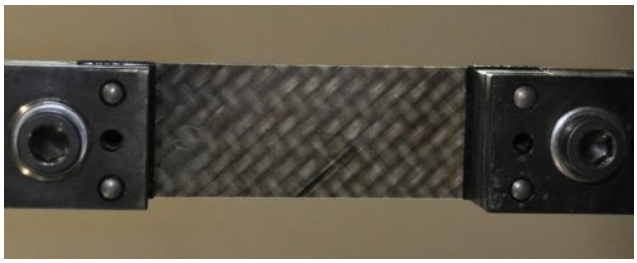

Fig. 45: Clamping device for the 36 mm specimen in the undeformed configuration.

reinforced matrices", say those materials in which one or more of the embedded phases are cocontinuous with the matrix in one or more directions. The above described fiber reinforced material is an example. A method to study effective properties of this kind of composites is presented in [67]. Effective properties are shown, in the framework of linear elasticity, estimable by using the global mean Green operator for the entire embedded fiber network which is by definition through sample spanning. This network operator is obtained from one of infinite planar alignments of infinite fibers, which the network can be seen

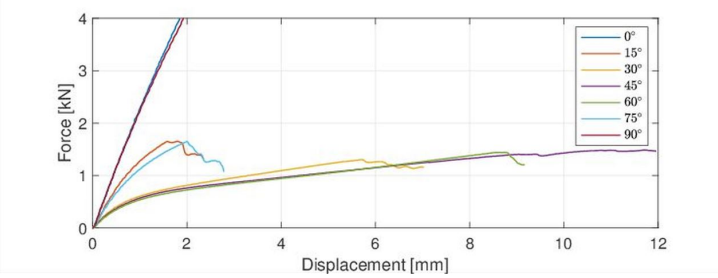

Fig. 46: Force-displacement curves for 25 mm specimens and different orientations of the fibers.

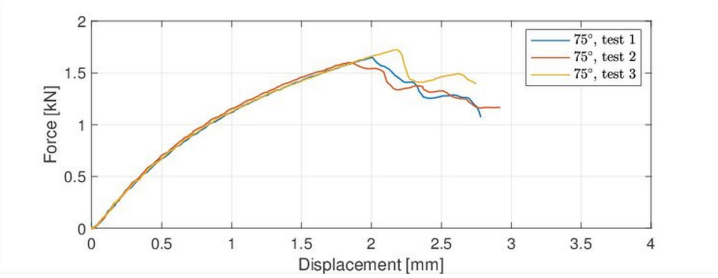

Fig. 47: Series of force-displacement curves for 25 mm specimens and 75° fiber orientation.

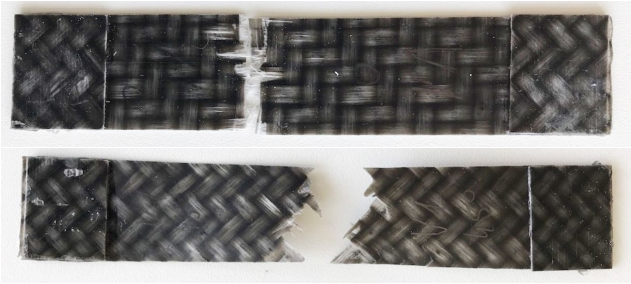

Fig. 48: Fracture patterns of the 25 mm specimen for 0° and 45° fiber orientations.

as an interpenetrated set of, with the fiber interactions being fully accounted for in the alignments. In [67] the effective properties of a planar alignement of fibers and of a 1D fiber bundle embedded in matrix are derived, but the same method can be generalized to be applied to pantographic-like fiber networks (see Fig. 49.

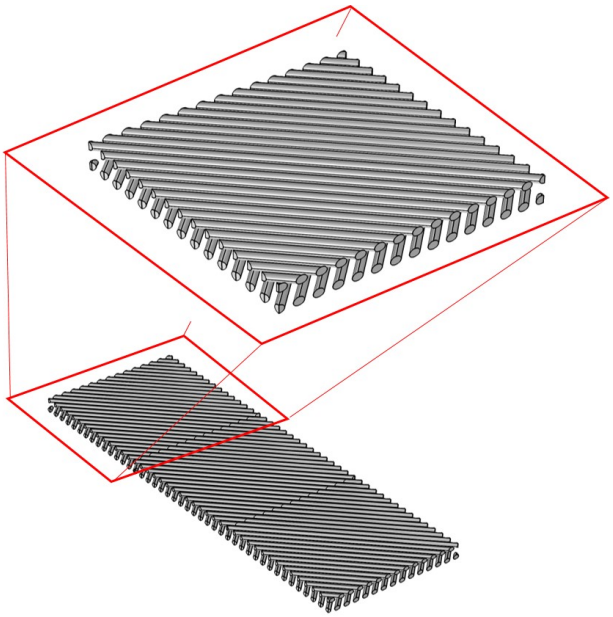

Fig. 49: Planar pantographic-like fiber network (the embedding matrix is hidden in the image). The pantographic arrangement can be obtained by considering two parallel fiber alignments with a relative disorientation of 90°

The effective properties obtained via the homogenization procedure can be evolved to obtain the behavior under deformation of the considered composite by introducing a dependence on some suitably chosen geometrical descriptor. In the 1D fiber bundle example, the evolution of the Young moduli and of the shear moduli are obtained in function of the parameter η related to the interdistance of the fibers (see Fig. 50). More details on the homogenization procedure based on the mean Green operators can be found in [68–70].

3.9 Wrinkling in engineering fabrics

The forming kinematics and mechanics of a 2×2 twill-weave carbon fabric (EasyComposites,product code = CF-22-20 0-150), treated with a speckle pattern for analysis using Digital ImageCorrelation (DIC) was characterized and reported in [71]. The width of warp and weft tows in the carbon fabric is 2.00 ± 0.01 and 1.92 ± 0.05 mm, respectively (Fig. 51). The mechanical forming properties were determined using a six-step procedure, discussed in-detail in [71, 72]. Several models exist to describe this kind of materials and their mechanical behaviors. Among them, in [72] two different 'comprehensive' modelling approaches are considered. These models, referred as "semi-discrete" and "continuum" models, are able to independently control the tensile, shear,

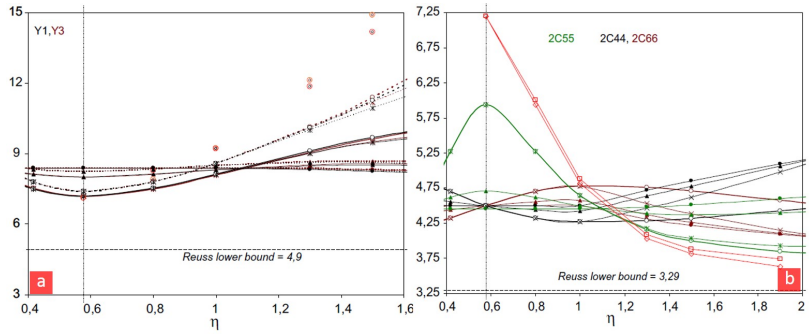

Fig. 50: Evolution with a stretch η of the three Young moduli (a) and shear moduli (b) for a 1D fiber bundle embedded in a softer matrix (four different extimates). The fiber volume fraction is 40%. Numerical 2D simulations for the in-plane shear modulus 2C55 reported for comparison are plotted as points linked by dashed straight red lines.

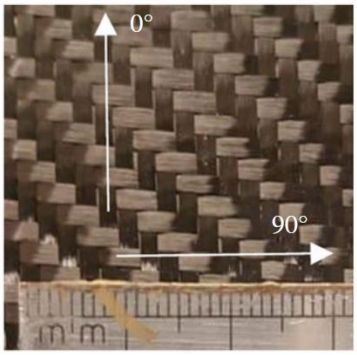

Fig. 51: Twill-weave carbon fabric showing warp (0°) and weft (90°) tows and scale rule.

out-of-plane bending, in-plane bending and torsional stiffnesses of the fabric, with the stiffnesses convecting with the fibre directions during large shear deformations. The semi-discrete model [71, 73] is based on the assumption that woven engineering fabrics can be modelled as a repeat unit cell, based on a pantographic module consisting of mutually constrained beam and membrane elements connected via zero-torque hinges. The continuum model is a second gradient continuum model. A comparison between the predictions obtained by using the two models and the experimental measures are reported in Fig. 52 for a uniaxial BIAS extension test.

The wrinkling of the engineering fabrics has been measured. Experimental results are shown in Fig. 53. To further emphasize this result, Fig. 54a displays

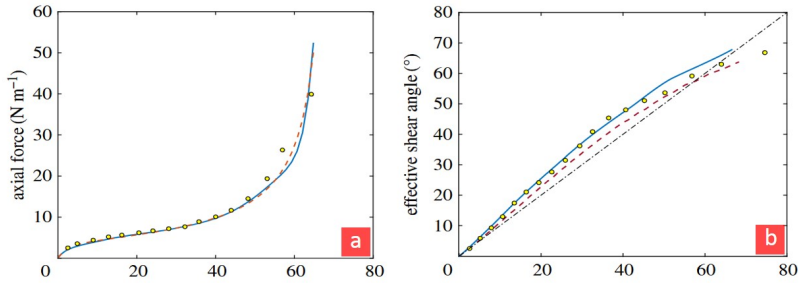

Fig. 52: Uniaxial Bias Extension test for the sample of size 150×300 mm. (a) Normalized axial force versus shear angle. (b) Effective shear angle versus ideal shear angle. The yellow dots indicate the experimental data, the blue continuum line the continuum model, the red dashed line the semi-discrete model.

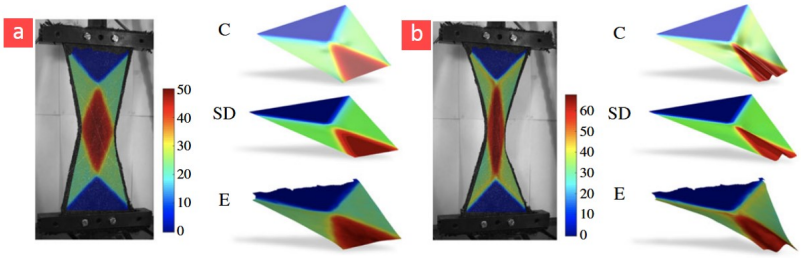

Fig. 53: Uniaxial Bias Extension test for the sample of size 150×300 mm. (E, experiment; SD, semi-discrete; C, continuum). Shear angle approximately (a) 50°, (b) 67°.

the out-of-plane displacement along a mid-section, cut parallel to the short edge of the sample, for different sizes of the samples. Fig. 54b shows the wrinkle amplitude versus the shear angle at the centre of the sample obtained by the continuum model; Fig. 55 shows the same plots obtained by the semi-discrete model. These figures allow to evaluate the wrinkle onset shear angles.

4 Image Analyses

4.1 Tomographic analyses

4.1.1 Low resolution aquisition: stainless steel and aluminum samples

Preliminary tomographic analyses have been carried out on a stainless steel pantographic structure. This type of analysis will be used in the future for the

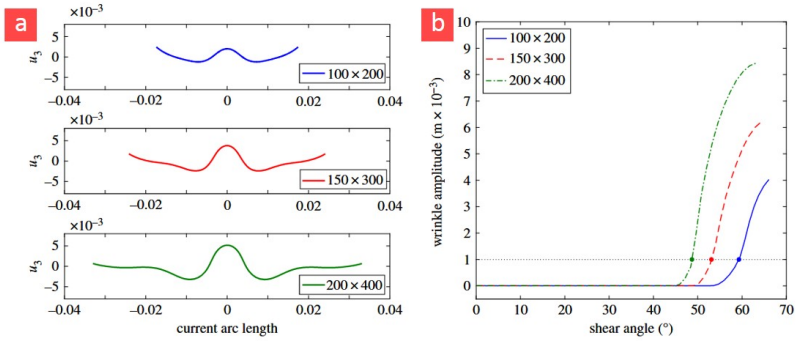

Fig. 54: Wrinkling details by continuum model. (a)Out-of-plane displacement along a mid-section for the samples 100×200, 150×300 and 200×400 with shear angles 64°, 67°and 68°, respectively. (b) Post buckling behaviour.

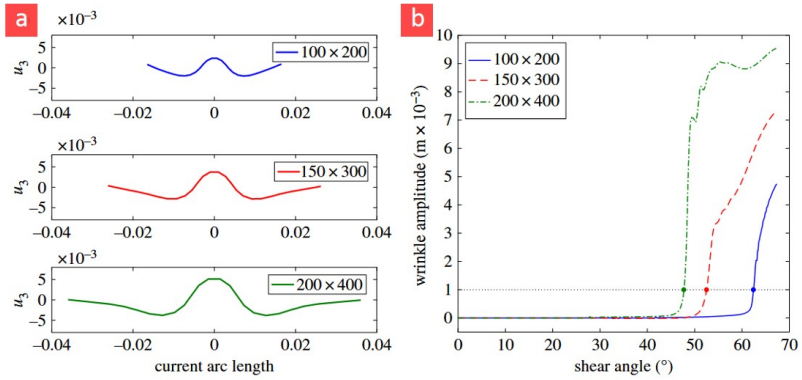

Fig. 55: Wrinkling details by semi-discrete model. (a)Out-of-plane displacement along a mid-section for the samples 100×200, 150×300 and 200×400 with shear angles 64°, 67°and 68°, respectively. (b) Post buckling behaviour.

understanding of microscopic mechanisms at the basis of damage and failure. The acquisition was conducted at low resolution inside a North Star Imaging X50+ tomograph, using a source setting of 170 kV, 600 μA and a 1536 × 1944 pixel panel detector. The physical voxel size is 69.5 μm in order to image the whole sample (Fig. 56a). 800 radiographs were acquired over the 360° of rotation with a frame average equal to 10. The acquisition frequency was 10 fps. The total duration of a single acquisition was approximately 30 minutes. A 0.5 mm thick copper filter was used. Fig. 56a shows the 3D rendering of a steel pantograph, and Fig. 56b a close-up view of a section showing the mesostructure.

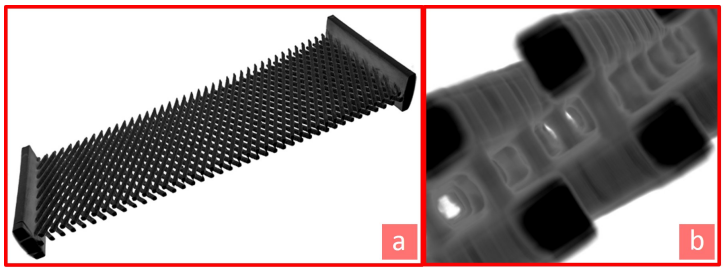

Fig. 56: 3D rendering of a 316L steel pantographic structure at macroscale and mesoscales.

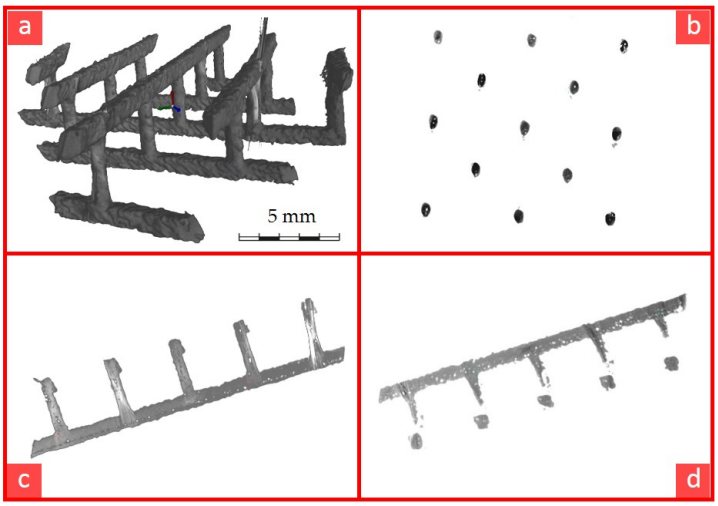

Fig. 57: Top left: μCT scan of the pantographic structure with a resolution of 5 μm. Top right: Cross section of pivot beams showing random porosities. Bottom left: Cross sections of lower fiber group, showing porosity accumulation on the downside. Bottom right: Cross sections of upper fiber group, showing porosity accumulation on the downside.

A single element of the successfully built specimens was analyzed by a μCT scan (see Fig. 57). Besides the rough surfaces, the images show an increased porosity within the material in comparison with bulkier parts. In particular, toward downskin areas, an accumulation of porosities is observed. These results indicate that further processing optimizations are necessary in order to create a material of high quality.

4.1.2 Polyamide and aluminum samples: microstructure visualisation

The microstructure of 3D printed polyamide and aluminum is investigated in the sequel. It was motivated by the potential to understand the microstructure of such materials to assess their applicability, effectiveness, and strength. 3D printed materials have the potential applications from manufacturing to bio-related fields [74, 75]. Micro X-ray Computed Tomography (μXCT) was used to obtain micrometer scale 3D microstructure of polyamide and aluminum samples obtained from pantographic specimen. The reconstructed μXCT images were used with the analysis software, Avizo, to obtain the porosity, specific surface area, and other statistics about the microstructure.

Micro X-ray CT imaging A Zeiss Micro X-ray CT machine was used to acquire the images (Zeiss Xradia 410 Versa 2018). The 10x lens objective was used to image the samples which results in a digital image with a square field of view of side $\approx$1.5$\times$103 μm and pixel size of $\approx$0.86 μm/pixels. A total of 1441 images at a frequency of 4 images per degree of rotation were acquired for tomographic reconstruction. The overall imaging time varied from 8-12 hours depending on the exposure time per image. Using the "Reconstructor" software, the radiographes were utilized to reconstruct the 3D volumes shown in Figs. 58 and 59. The reconstructed 3D structure has a voxel size of 1.72x1.72x1.72 μm^3. A visual inspection of the reconstructed structure reveals a smooth internal microstructure for the aluminum with spherical pores of varying sizes. This observation is not unexpected since the SLM process was used for its fabrication. Conversely, the polyamide internal structure has a granular structure formed by the sintering of the polyamide grains in the SLS process. In addition, the pores in polyamide have irregular shapes, suggesting that the polyamide powder grains do not lose completely their original shape during sintering as they would do in a melt. The sintered internal microstructure formed in this way will lead to properties that are different than polyamide formed by melting and solidifying the powder.

3D Analysis A porosity analysis was performed using the wizard and image segmentation tool of Avizo (9.5.0 software). To ensure that the segmentation tool identifies the interior pore spaces, the reconstructions were cropped down to cubes to avoid irregular boundary effects. Figures 60a and 60b illustrate the boundary irregularity in the original reconstruction for polyamide and aluminum specimens, respectively, shown as selected sections in xy-, xz-, yz-planes and the 3D solid, respectively. Multiple cubic sub-volumes were taken from different locations of the original reconstruction to ensure that the major topographic features (i.e. pore spaces) of the original reconstruction were represented.

Figures 61 and 62 give 3 instances of the cubical samples for polyamide specimen of size 250$\times$250$\times$250 voxels shown as selected sections in xy-, xz-, yz-planes and the 3D rendering, respectively. From Figs. 61 and 62, we can see that the pores in these specimen were characterized by a large aspect ratio.

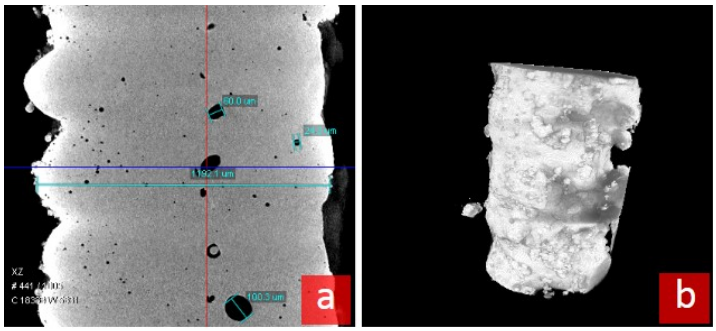

Fig. 58: Reconstructed 10x aluminum alloy SLS-made (part of) pantographic structure.

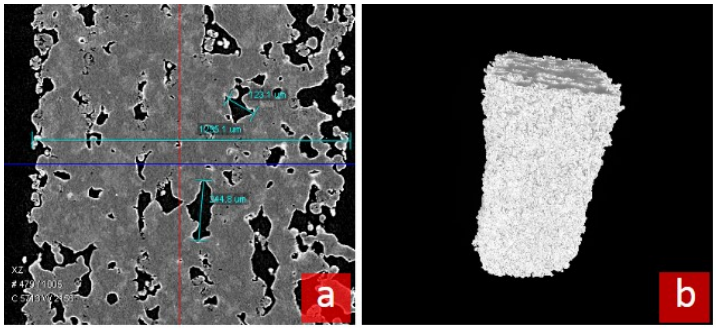

Fig. 59: Reconstructed 10x polyamide SLS-made (part of) pantographic structure.

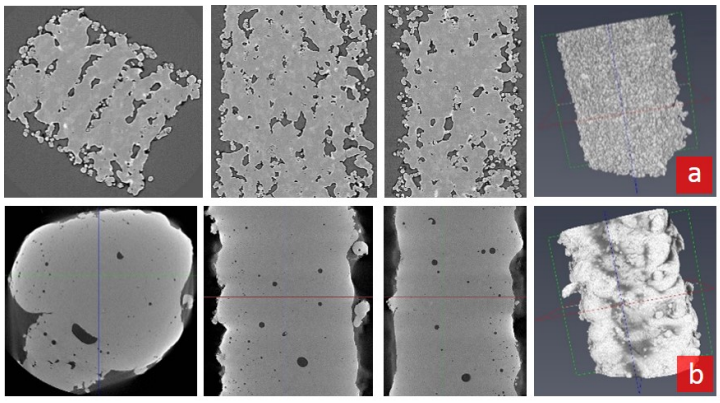

Fig. 60: Selected sections in xy-, xz-, yz-planes and the 3D rendering of the analyzed volume, respectively of the original reconstructed μXCT image for (a) polyamide and (b) aluminum specimens, showing irregular boundaries.

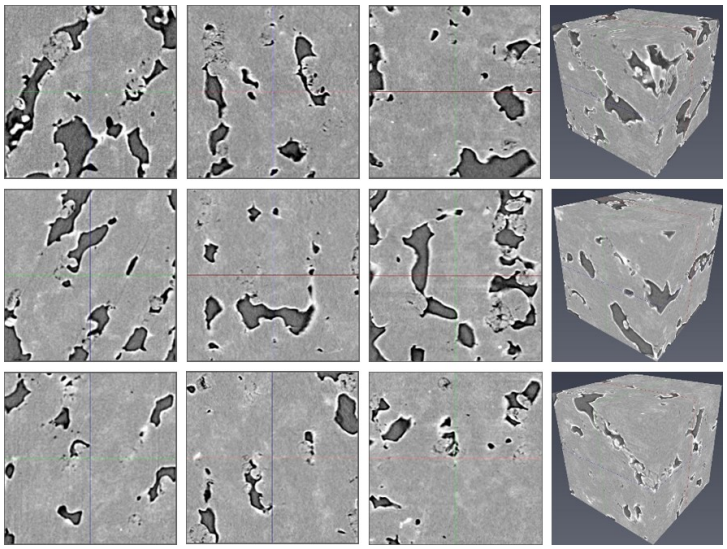

Fig. 61: The columns give selected sections in xy-, xz-, yz-planes and the 3D rendering of the analyzed volume, respectively for 3 cubic samples (rows) cropped from the top, middle and lower regions of the original reconstructed μXCT image for the polyamide specimen.

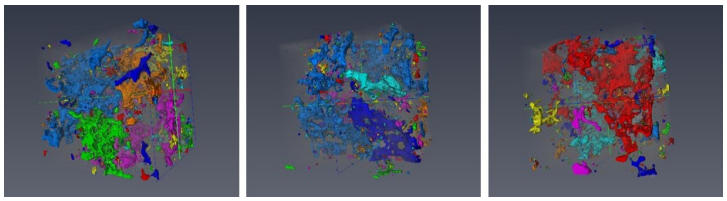

Fig. 62: The pore structures with 3 cubic samples cropped from the top, middle and lower regions of the original reconstructed μXCT image for the polyamide specimen. The irregular shapes with large aspect ratio of the pore spaces can be seen.

These pores are typically aligned such that there larger dimensions are aligned in the z-direction that is orthogonal to the build direction of the SLS process. The average porosity of the aluminum specimen was found to be 6.5%.

Figures 63 and 64 give 3 instances of cubic samples for aluminum specimen of size 400x400x400 voxels shown as selected sections in xy-, xz-, yz-planes and the 3D solid, respectively. The cubical sample sizes were predicated by the original cross-sectional dimensions of the beam specimens and their orientation in the xy-plane. From Figs. 63 and 64, we can see that the pores in these specimen mostly spherical.

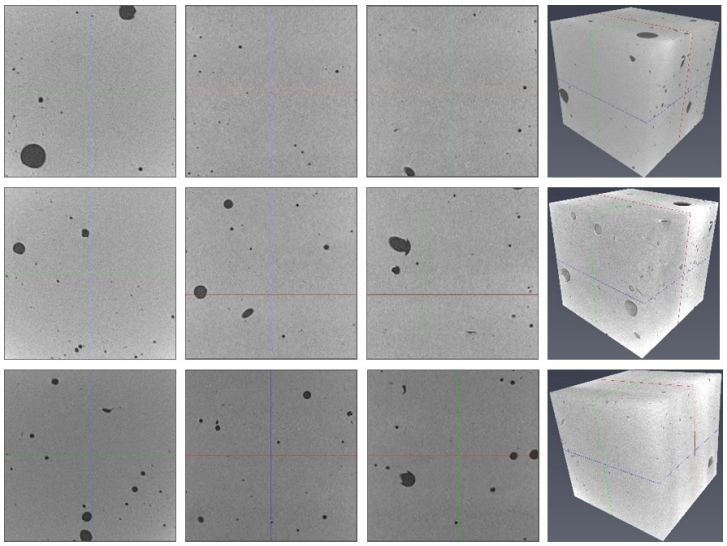

Fig. 63: The columns give selected sections in xy-, xz-, yz-planes and the 3D rendering of the analyzed volume, respectively for 3 cubic samples (rows) cropped from the top, middle and lower regions of the original reconstructed μXCT image for the aluminum alloy specimen.

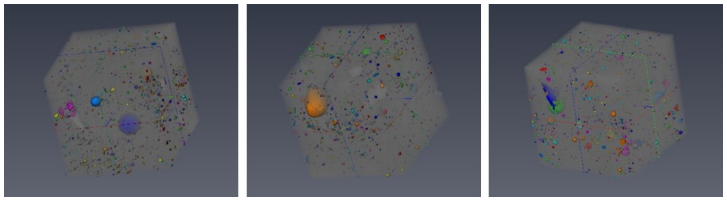

Fig. 64: The pore structures with 3 cubical samples cropped from the top, middle and lower regions of the original reconstructed μXCT image for the aluminum alloy specimen. The mostly spherical shapes of the pore spaces can be readily seen.

Avizo's segmentation tool was used to define the labels of the material volume versus the pore volume in the cropped sub-volumes. Once the areas were defined, Avizo's label analysis tool was used to calculate the volume statistics. The porosity analysis wizard was also used to obtain the pore size distribution. The average porosity of the polyamide sample was calculated to the 18.5%. For polyamide specimen, the maximum pore size varied from 573 μm to 640 μm, while the median pore size ranged from 6 μm to 7 μm for the 3 sub-volumes samples. For aluminum specimen, the maximum pore size varied from 168 μm to 195 μm, while the median pore size ranged from 5 μm to 8 μm for the 3 sub-volumes.

4.2 Principle of Digital Image Correlation

Digital Image Correlation (DIC [76,77]) can be used to quantify evolution of displacement field at prescribed resolution of a deformed specimen. Recently, this technique has been applied to extract the displacement fields as the pantographic structure is deformed in the experimental tests [45,14]. For the pantographic structures, displacement fields can be derived at macroscopic and mesoscopic scales. These displacement fields can then be compared with those predicted via numerical simulations. By this comparison it is possible to validate the considered constitutive model.

DIC is based upon the analysis of digital images of surfaces at different stages of deformation in experiments, with an aim to obtain a precise estimation of the deformations. One of the limits of DIC comes from its ill-posedness. Generally, only limited information is available from gray level images. For this reason, it is not possible to measure displacement fluctuations beyond certain spatial resolution. Consequently, it is necessary to find a compromise between the uncertainty level and the spatial resolution [78]. Unrefined descriptions of displacement fields based on discretizations coarser than the scale of pixels are usually required. Additional information is necessary to achieve finer resolutions. For example, it is possible to consider continuous displacement fields and decompose them on convenient kinematic bases (e.g., finite element shape functions). The calculation time is increased in this global approach, but the uncertainties can be lowered [78].

4.2.1 Global DIC

The registration of two gray level images in the reference (f) and deformed (g) configurations is based on the conservation of gray levels

$$f\left(\boldsymbol{x}\right) = g\left(\boldsymbol{x} + \boldsymbol{u}\left(\boldsymbol{x}\right)\right) \tag{3}$$

where $\boldsymbol{u}$ is the (unknown) displacement field to be measured and $\boldsymbol{x}$ the position of pixels. The sought displacement field minimizes the sum of squared differences Φ_c^2 over the region of interest (ROI)

$$\Phi_c^2 = \sum_{\mathrm{ROI}} \varphi_c^2(\boldsymbol{x}) \tag{4}$$

where φ_c defines the gray level residuals $\varphi_c(x) = f(\boldsymbol{x}) - g(\boldsymbol{x} + \boldsymbol{u}(\boldsymbol{x}))$ that are computed at each pixel position $\boldsymbol{x}$ of the ROI. The minimization of Φ_c^2 is a nonlinear and ill-posed problem. This is the reason for considering a weak formulation in which the displacement field is expressed over a chosen kinematic basis

$$\boldsymbol{u}(\boldsymbol{x}) = \sum_n \boldsymbol{u}_n \boldsymbol{\psi}_n(\boldsymbol{x}) \tag{5}$$

where $\boldsymbol{\psi}_n$ are vector fields and u_n the associated degrees of freedom, which are gathered in the column vector $\boldsymbol{u}$. Thus the measurement problem consists in the minimization of Φ_c^2 with respect to the unknown vector $\boldsymbol{u}$. This problem is nonlinear and to obtain a solution Newton's iterative scheme can be implemented.

In the following analyses, the vector fields correspond to the shape functions of 3-noded triangular elements (i.e., T3 elements). Consequently, the unknown degrees of freedom are the nodal displacements of the T3 elements.

4.2.2 Regularized DIC

The previous approach can be penalized when the image contrast is not sufficient to achieve low spatial resolutions. This is, for instance, the case in the analyses reported hereafter. Regularization techniques can then be selected [79]. They consist of adding to the global correlation functional Φ_c^2 penalty terms. In the following, a first penalty, which is based on the local equilibrium gap, is added for the inner nodes of the finite element mesh and those belonging to the free edges

$$\Phi_m^2 = \{\mathbf{u}\}^\top [\mathbf{K}]^\top [\mathbf{K}] \{\mathbf{u}\} \tag{6}$$

where $[\mathbf{K}]$ is the rectangular stiffness matrix restricted to the considered nodes. For the other edges, a similar penalization is considered

$$\Phi_b^2 = \{\mathbf{u}\}^\top [\mathbf{L}]^\top [\mathbf{L}] \{\mathbf{u}\} \tag{7}$$

where $[\mathbf{L}]$ is a second operator acting on the nodal displacements of the boundaries that are not traction-free [**?**].

The global residual to minimize then consists of the weighted sum of the previous three functionals (i.e., Φ_c^2,Φ_m^2 and Φ_b^2). Because the dimensions of the first functional is different from the other two, they need to be made dimensionless. It follows that the penalization weights acting on Φ_m^2 and Φ_b^2 are proportional to a regularization length raised to the power 4 [79]. The larger the regularization length, the more weight is put on the penalty terms. This penalization acts as a low-pass mechanical filter, namely, all high frequency components of the displacement field that are not mechanically admissible are filtered out. Similarly, for low-contrast areas mechanical regularization provides the displacement interpolation. The following analyses illustrate the benefit of using DIC to measure displacement fields at the macroscopic and mesoscopic scales.

4.2.3 DIC applied to pantographic structures

Application to a BIAS extension test In the following, a BIAS extension test performed on a steel pantographic structure is analyzed. In total, a series of 55 pictures will be analyzed for which no damage was observed. Figure 65 shows the picture of the initial configuration, and three loaded configurations

corresponding to the 17th, 34th and 51st studied steps. In the present case, the pivots of the pantograph were marked in black, and a random pattern was created by spraying black and white paint on the grips. The fact that the grips were patterned helps the DIC code to converge even though very large displacement levels occur during the experiment.

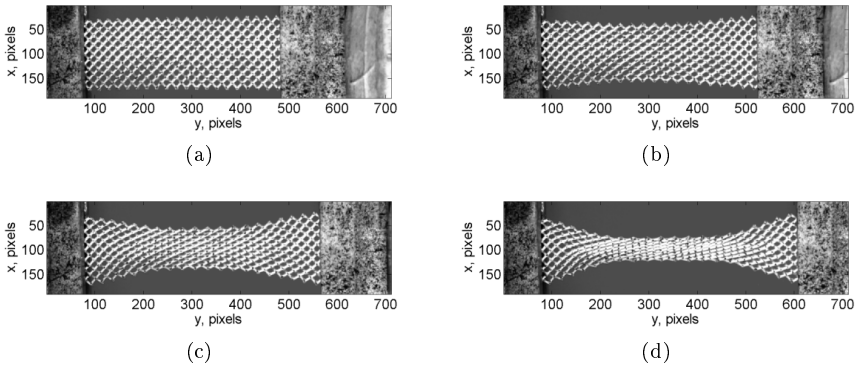

Fig. 65: Gray level images of the pantograph in the reference configuration (a), 17th (b), 34th (c) and 51st (d) loading steps

Macro- and mesoscale analyses will be reported in the sequel. For macroscale analyses, the rectangular region of interest was meshed with T3 elements independently of the underlying mesostructure. Such discretizations may then be compared with numerical simulations performed at the macroscale [14]. Four different mesh densities were considered (Fig. 66(a-d)). The characteristic mesh size, which is defined as the square root of the average element surface, was equal to 28 pixels for the first mesh, 13 pixels for the second one, 8 pixels for the third one, and 6 pixels for the last. These four meshes will be utilized for convergence analyses of the DIC results at the macroscale.

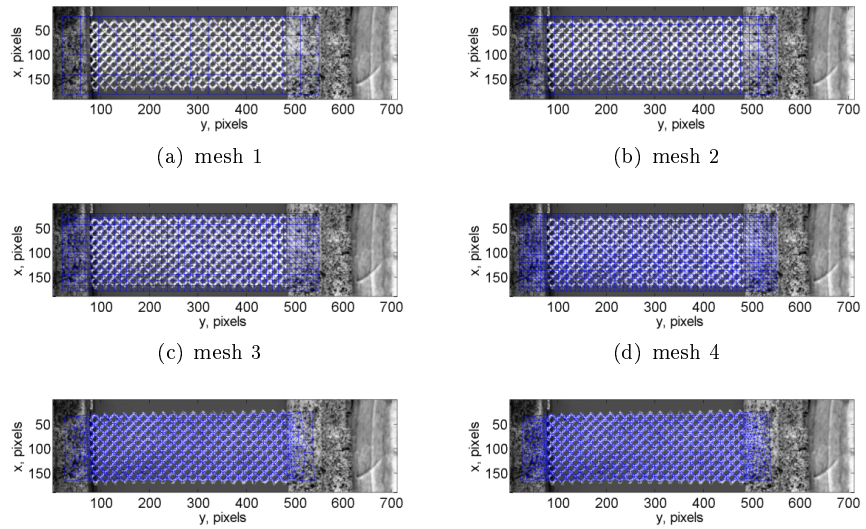

(a) mesh 1 (b) mesh 2

(c) mesh 3 (d) mesh 4

(e) mesh 5 (f) mesh 6

Fig. 66: Finite element meshes overlaid with the gray level picture of the reference configuration.

Two additional meshes were tailored to the pantograph mesostructure (Fig. 66(e-f)). Contrary to the polyamide pantograph for which simple morphological operations were performed in order to construct the mesoscale mesh from a mask [14], the procedure was different herein. The starting point was the nominal geometry of the pantograph, which would be used, say, in FE simulations. From this information, the mesh was created with Gmsh [80] (Fig. 67(a)) and a picture of the corresponding mask (Fig. 67(b)). A DIC analysis was run between the reference picture and the mask to deform it so that the mesh can be backtracked onto the actual pantograph surface. In such an analysis, an auxiliary (coarse) mesh was used (Fig. 67(c)). Once the DIC analysis converged, the original mesh was consistent with the actual geometry of the pantograph (Fig. 67(d)).

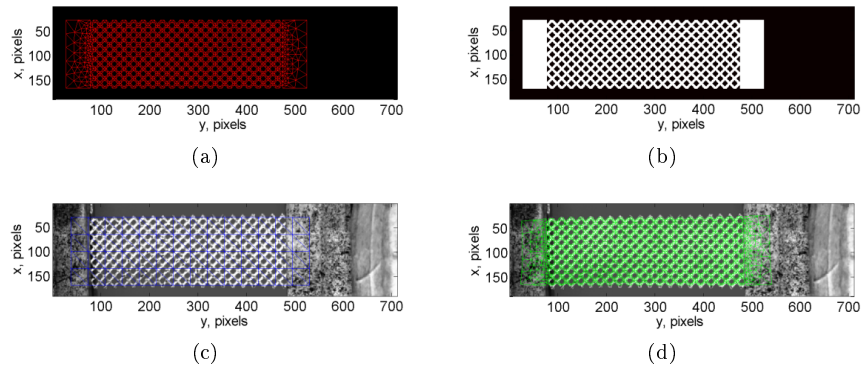

Fig. 67: Illustration of the back-tracking procedure. Initial mesh (a) and corresponding mask (b). (c) Reference picture and mesh used to register the mask. (d) Overlay of back-tracked mesh and reference picture.

This back-tracking procedure was applied to two meshes (Fig. 67(e-f)). The corresponding characteristic mesh size is equal to 3.7 and 3.6 pixels, respectively. It is worth noting that such discretizations can only be considered thanks to regularization techniques since the correlation length of the pantographic structure is of the order of 10 pixels. Only so-called direct calculations will be reported in which each considered picture is registered with respect to the reference image. To speed-up convergence, a first incremental analysis is run in which the reference configuration becomes the deformed configuration of the previous analysis step. These first results are used as initialization to the direct registrations. The regularization length was chosen equal to 30 pixels. The convergence condition on the norm of the mean displacement correction was set to 10^{-3} pixel, which is very low since the measured displacement amplitudes will be significantly higher (*i.e.,* more than 130 pixels in the longitudinal directions, and $\pm$ 50 pixels in the transverse direction).

In global DIC, the registration quality is assessed with gray level residual fields, which correspond to the pixel-wise gray level difference between the picture in the reference configuration and the picture in the deformed configuration corrected by the measured displacement. The quantity to be minimized is the L2-norm of the gray level residuals over the region of interest [77]. The root mean square (RMS) level is reported in Fig. 68 for all six meshes considered herein. The first general tendency is that the registration quality degrades as more steps are analyzed, thereby signaling that the measured fields become very complex at the end of the experiment (Fig. 65). Such type of observation wa already made for the polyamide pantograph [45,14]. Second, there is a significant difference between the first four meshes and the last two. This proves that meshes tailored to the actual pantograph surface better capture the kinematics of the test, even with the same regularization length as for coarser meshes. Third, in both cases, a converged solution is obtained in

terms of mesh density with respect to the chosen regularization length. More precisely, meshes 3 and 4 at the macroscale, meshes 5 and 6 at the mesoscale have the same residual levels. Consequently, there is no need to further refine the discretization with the chosen regularization length.

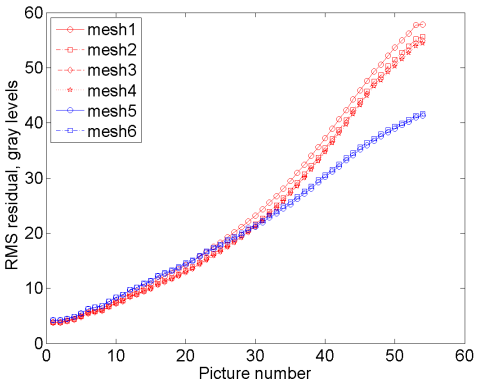

Fig. 68: RMS gray level residual as functions of the picture number for the six meshes shown in Fig. 66.

In the following discussion, only two sets of results are reported, namely, those of meshes 4 (at the macroscale) and 6 (and the mesoscale). Figure 69 shows the longitudinal and transverse displacements measured for the 17th picture. The transverse displacement field u_x shows a very important contraction, which is of the same order of magnitude as the longitudinal motions u_y. Since the width of the sample is one third of its length, the transverse deformations are much more important than the longitudinal component. This observation applies to both scales. In the present case, both measurements have approximately the same quality in terms of overall registration residuals (Fig. 68).

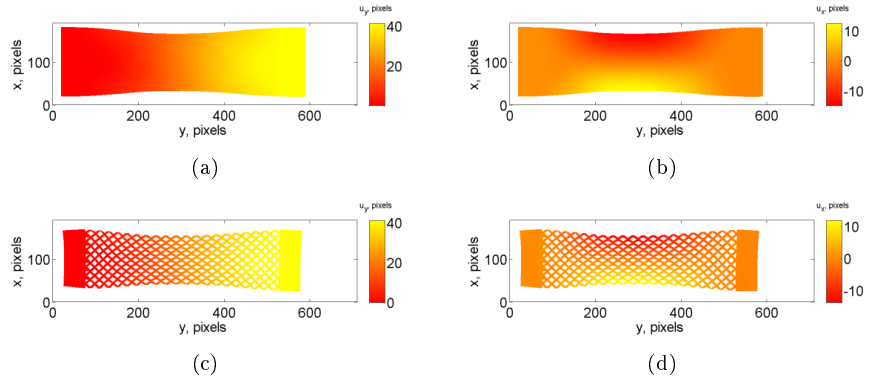

Fig. 69: Longitudinal (a-c) and transverse (b-d) displacement fields measured with meshes 4 (a-b) and 6 (c-d) for the 14th picture. The fields are shown on the deformed configuration.

In Fig. 70 the same fields are shown for the 34th picture. The main features of the transverse and longitudinal displacement fields are identical to the previous step, yet with higher overall levels. The displacement ranges still are of the same order of magnitude for the longitudinal and transverse displacements. Consequently the central part of the sample is thinner. The deformed shapes are very close for both meshes, which translates into the same levels of registration residuals (Fig. 68).

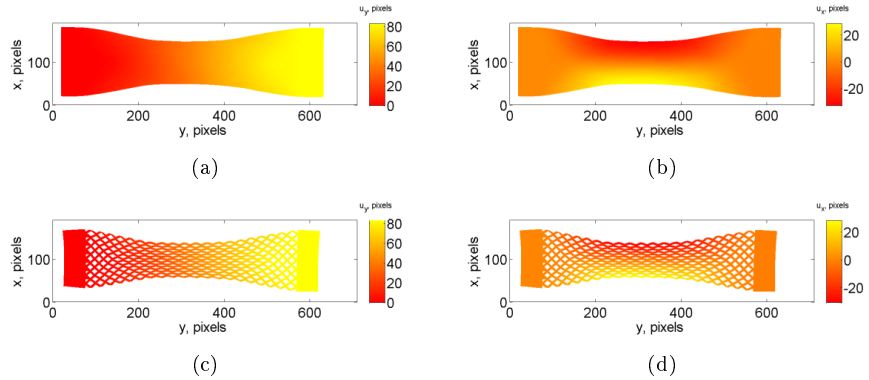

Fig. 70: Longitudinal (a-c) and transverse (b-d) displacement fields measured with meshes 3 (a-b) and 4 (c-d) for the 34th picture. The fields are shown on the deformed configuration.

One of the last steps is reported in Fig. 71. In that case the gray level residuals (Fig. 68) are significantly higher for mesh 4 (at the macroscopic scale)

in comparison with mesh 6 (at the mesoscopic scale). There is a clear difference in the deformed shape whose width is lower for the mesoscopic analysis in comparison with the macroscopic result. The highly deformed region has grown toward both ends of the pantographic sheet, which can be understood by the fact that when struts touch each other, the deformation mechanism moves away from these zones.

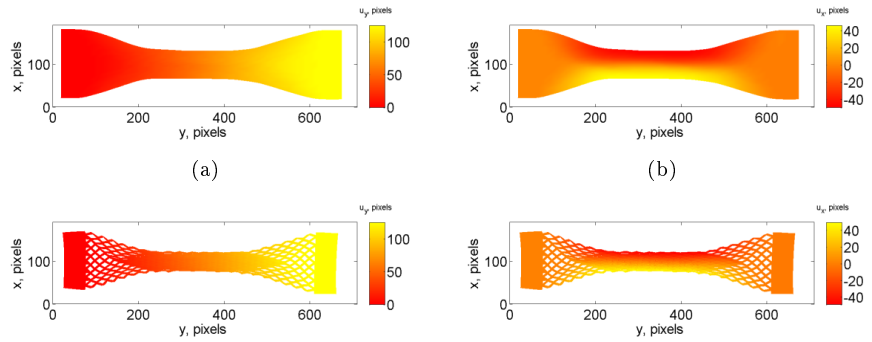

(a) (b) (c) (d)

Fig. 71: Longitudinal (a-c) and transverse (b-d) displacement fields measured with meshes 3 (a-b) and 4 (c-d) for the 51th picture. The fields are shown on the deformed configuration.

The results reported herein confirm that DIC analyses can be run on pantographic structures at macroscopic scales [45,14] and mesoscopic levels [14] with regularized DIC on very fine meshes (*i.e.,* down to 3.6 pixel elements). Important gains were observed in terms of registration quality by moving from the macroscopic to the mesoscopic scale (*i.e.,* more than a factor of one and a half at the end of the picture series). The final gray level residuals indicate that even more advanced approaches should be followed. What is missing in the mesoscopic analysis is the special kinematics provided by the pivots.

Application to a shear test Shear tests have also been reported for pantographic structures [39]. This second example deals with 1,000 pictures with an 8-bit digitization and a definition of 1388×1038 pixels. The physical size of one pixel is equal to 110 µm. The first part of the experiment was monitored very finely, and then the acquisition rate was decreased (Figure 72(a)).

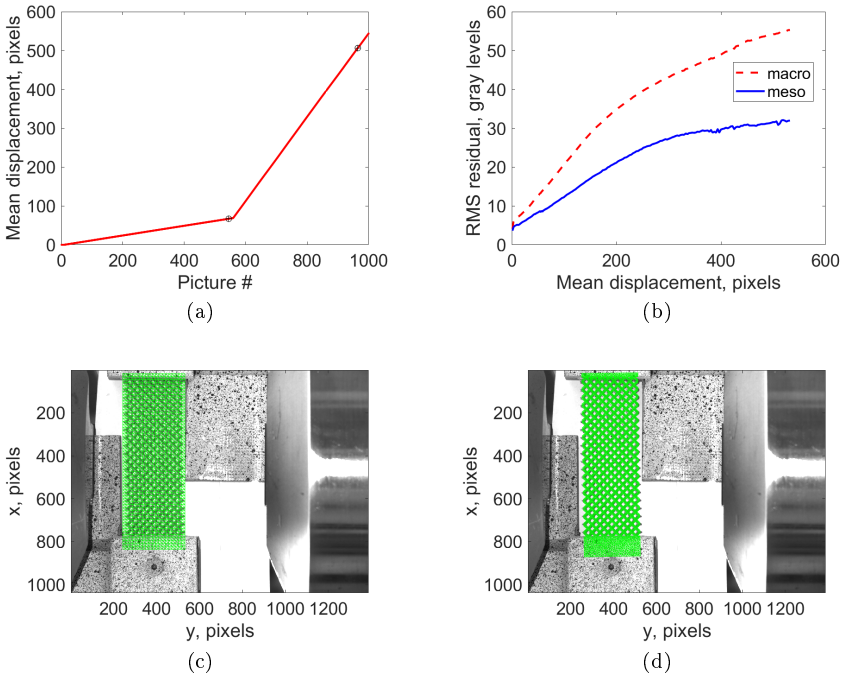

Fig. 72: (a) Mean transverse displacement of the crosshead. The black symbols depict the two states that are analyzed hereafter. (b) RMS gray level residuals for the whole image sequence. Meshes at the macro- (c) and meso- (d) scales overlaid on top of the image of the reference configuration.

In the following DIC analyses, the two scales of measurements are discussed. The mesh at the macroscopic level encompasses the whole pantograph and a small part of the grips (Figure 72(c)). The mean characteristic mesh size was equal to 10 pixels. Conversely, the mesh at the mesoscale only covers the external surface of the pantograph (Figure 72(d)). Its characteristic size was equal to 5 pixels on average. It was backtracked by following the same procedure as in the BIAS test. In the present case, the regularization length was equal to 75 pixels (*i.e.* higher than in the previous case) since the regularization strategy was now applied to incremental displacements (*i.e.* Hencky-type elasticity) and not to total displacements. When studying the gray level residuals, there is a gradual degradation as the applied displacement increases. This trend shows that the selected kinematic bases are regularization strategy are not able to fully describe the experiment. Contrary to the previous, there are clearer differences between macroscopic and mesoscopic kinematic bases, namely, the former leading to higher residuals than the latter.

Figure 73 shows the displacement fields measured for the 545-th picture (Figure 72(a)), which are overlaid on top of the picture in the deformed con-

figuration. Even though the gray level residuals were higher than those at the very early stages of the experiment (Figure 72(b)), the results are still reasonably consistent with the underlying mesostructure. In terms of overall pattern, the mesoscopic and macroscopic fields are close.

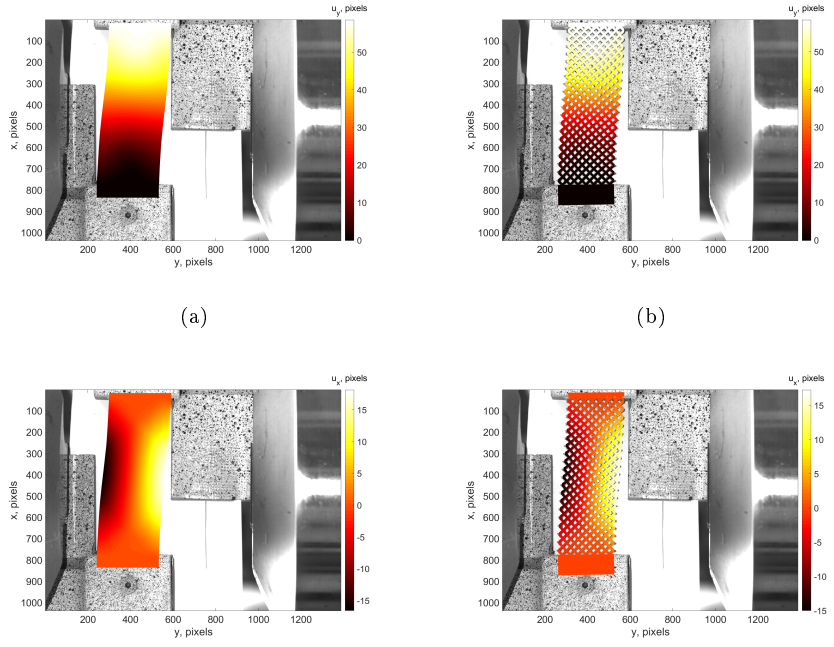

Fig. 73: Transverse (a-b) and longitudinal (c-d) displacement fields measured with macro (a-c) and meso (b-d) meshes for the 545th picture. The fields are overlaid on top of picture in the deformed configuration.

The gray level residual fields are reported in Figure 74 for the two types of discretizations. Significant differences are observed between the two fields. The mesostructure appears in the residuals of the macroscopic calculations (Figure 74(a)). This observation proves that the macroscopic kinematics does not fully capture the actual sample deformation. Conversely, the mesoscopic kinematics better describes the underlying deformation process. As a consequence, the gray level residuals are lower than those observed with the macroscopic mesh (Figure 74(b)).

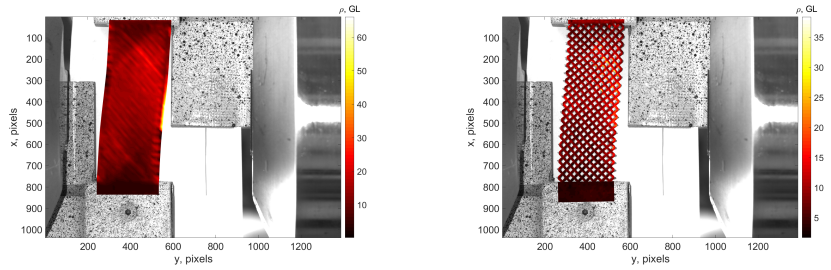

(a) (b)

Fig. 74: Gray level residual fields with the macro (a) and meso (b) meshes for the 545th picture. The fields are overlaid on top of picture in the deformed configuration.

Green Lagrange strain fields are reported in Figure 75 for both discretizations. It is interesting to note that even though elastic regularization was considered, some details of the mesostructure appear in the macroscopic fields associated with the normal strain components (Figure 75(a,c). The shear strain levels (Figure 75(e) remain rather small in comparison with the normal strain amplitudes (Figure 75(a,c)). The mesoscopic mesh, which is more closely related to the underlying mesostructure, enables higher strain magnitudes to be measured in comparison with the macroscopic discretization.

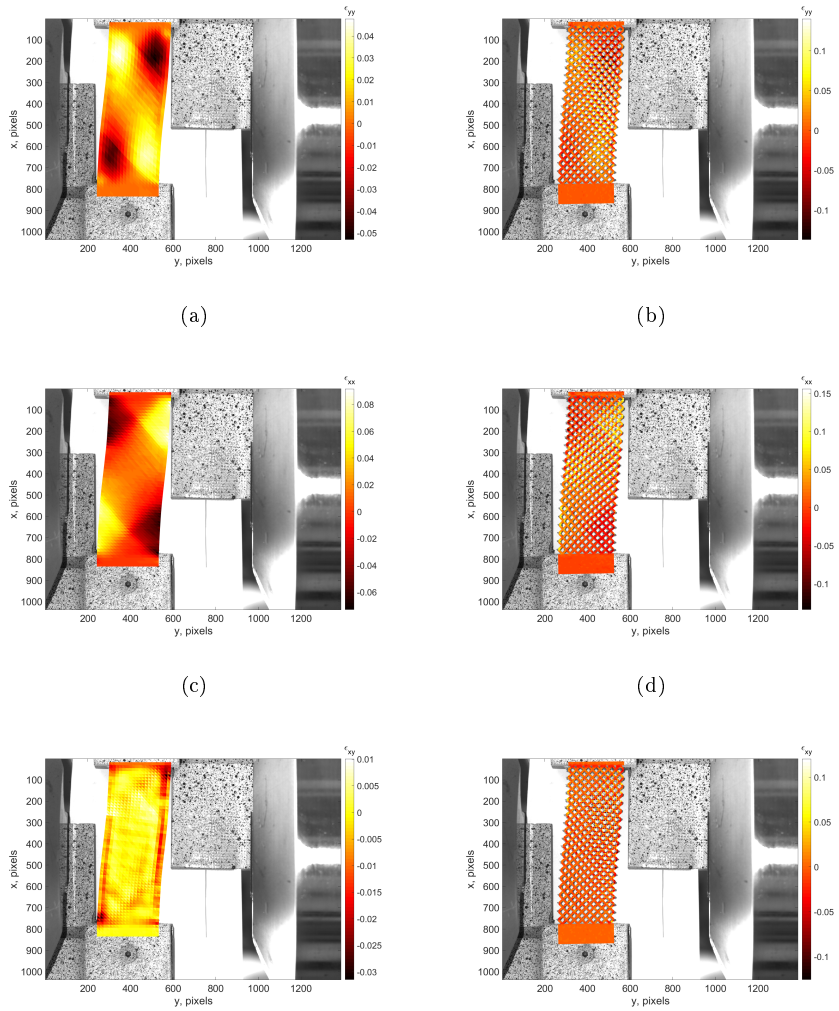

Fig. 75: Normal transverse (a-c), longitudinal (b-d) and shear (e-f) strain fields measured with macro (a-c) and meso (b-d) meshes for the 545th picture. The fields are overlaid on top of picture in the deformed configuration.

One of the last step of the experiment (*ie* 965-th picture, see Figure 72(a)) is now analyzed. This configuration is significantly deformed and leads to a crosshead displacement level greater than 60 % of the sample height. The displacement field pattern is again similar for macroscopic (Figure 76(a,c)) and mesoscopic analyses (Figure 76(b,d)).

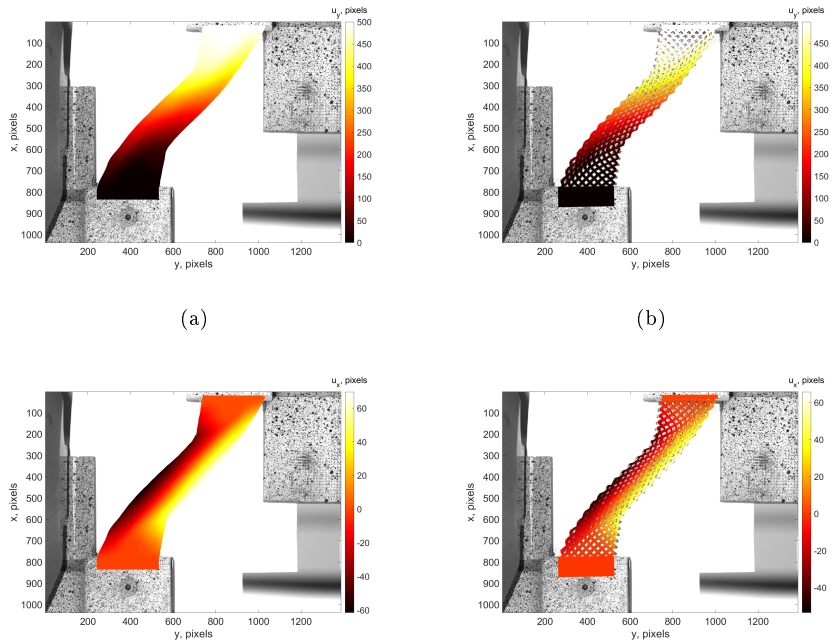

Fig. 76: Longitudinal (a-c) and transverse (b-d) displacement fields measured with meshes 3 (a-b) and 4 (c-d) for the 965th picture. The fields are shown on the deformed configuration.

The gray level residual field corresponding to the macroscopic discretization (Figure 77(a)) indicate that the kinematic description is too crude to properly capture local details. This phenomenon leads to overall levels that are about two times higher than the mesoscopic analysis (Figure 72(b)). At the end of the analysis, the mesoscopic mesh and corresponding discretization of the displacement field is more trustworthy than the macroscopic mesh. Even though the mesoscopic mesh is better suited, it still does not fully capture the actual deformation (Figure 77(b)). An even more detailed description is need (*eg* describing the local kinematics around pivots).

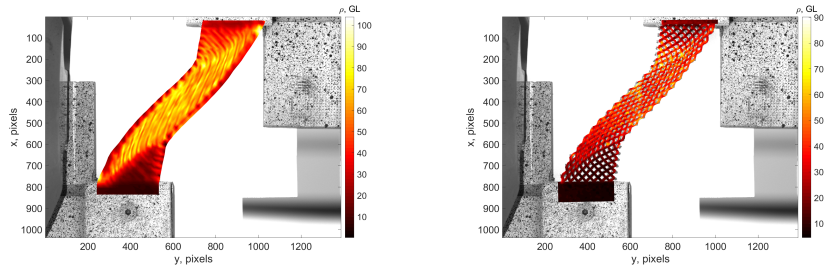

(a) (b)

Fig. 77: Gray level residual fields with the macro (a) and meso (b) meshes for the 965th picture. The fields are overlaid on top of picture in the deformed configuration.

Green Lagrange strain fields are shown in Figure 75 for the two different discretizations. Signification differences are observed in any of the reported fields, except in the areas close to the grips where the pantograph does not deform too much. It is worth noting that the strain levels are higher with the mesoscopic mesh in comparison with the macroscopic discretization.

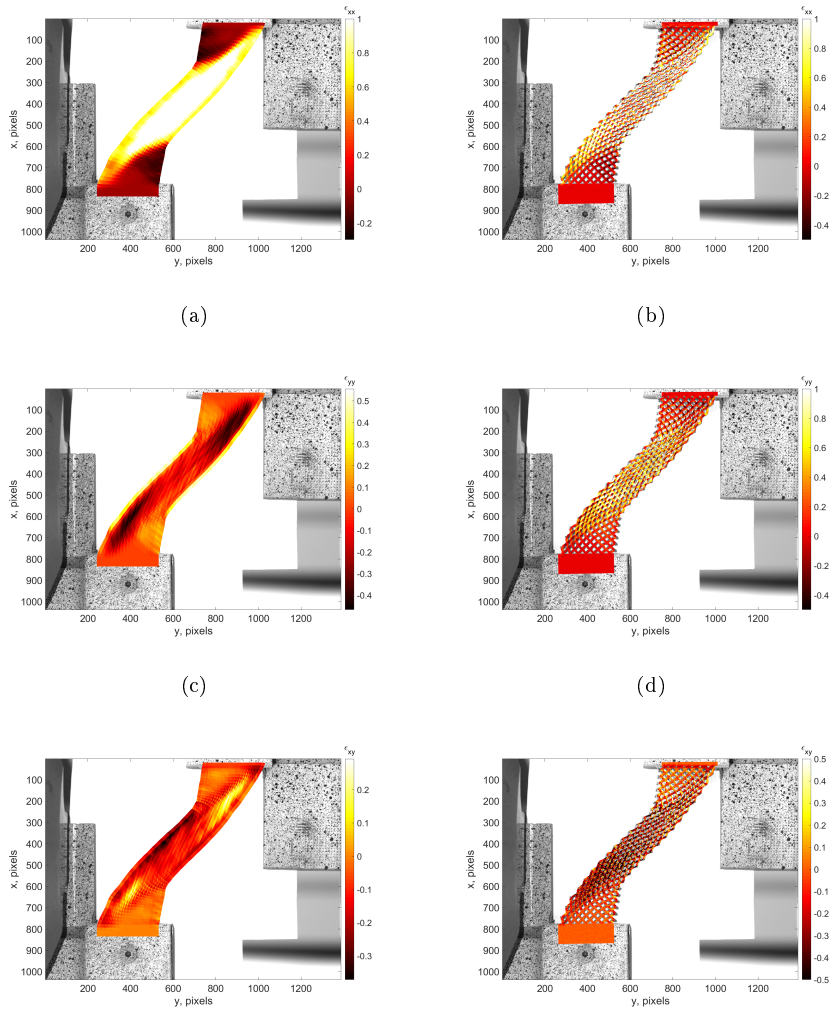

Fig. 78: Normal transverse (a-c), longitudinal (b-d) and shear (e-f) strain fields measured with macro (a-c) and meso (b-d) meshes for the 965th picture. The fields are overlaid on top of picture in the deformed configuration.

4.3 Digital image correlation for fiber reinforced pantographic-like materials

For the digital image correlation measurements of the fiber reinforced material, the optical system Q400 from Limess & Software GmbH has been used. The subsequent evaluation of the images has been done in Instra4D, version 4.1.

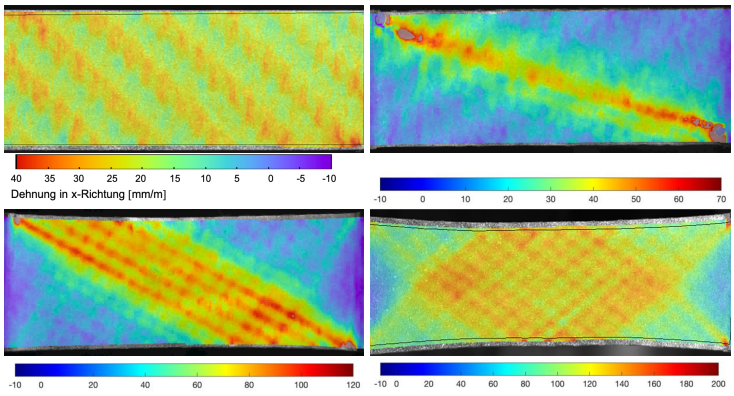

Fig. 79: Strain measurements in horizontal direction via DIC, all data in [mm/m]. Fiber directions are presented from left to right, top to down: [90°, 75°, 60°, 45°].

For the analysis, Instra4D generates a cloud of points within the region of interest (ROI) with a spacing of 5 pixels. At each point, a facet of 29 pixels has been applied, i.e. each facet is slightly larger compared to a single segment of the correlation cloud. To control the calculated strains, the position of each identified object in the current configuration has been calculated back into the reference configuration and compared with the original picture with a maximum tolerance of 0.3 pixel.

The results for the 36 mm specimen are given in Fig. 79. They are displayed here to highlight the effects of the fiber reinforcement, whereas the 25 mm specimens are more suitable for investigations on boundary effects. In Fig. 79 the results for 90°, 75°, 60° and 45° fiber orientations are shown. For the 90° direction, the patterns of the woven fabric can be recognised, where the 90° denotes the weft and 0° the warp direction. The resulting stiffness due to the periodically arising junctions, connecting the warp and weft directions of the fibers, is responsible for this kind of pattern.

For the 75° direction, the fibers in the warp direction are aligned in the 15° direction. For this set up, the fibers connecting diagonally the clamping devices carry a major portion of the external load. As can be seen in Fig. 79, upper right picture, the laminate already starts to fracture near the clamps, leading to a heavily reduced strength as reported in Fig. 46. Using the 60° direction as shown in the lower left picture of Fig. 79, the fibers cannot connect the clamping devices directly, leading to a stress redistribution to a couple of fibers. To redistribute the stress between the active, i.e. the external load carrying fibers, the connecting junctions play a major role. Lastly, the lower right picture demonstrates the effects of the pantographic-like structure. Compared to the results presented in Fig. 16, shows that nearly identical strain patterns arise.

5 Conclusion

The spirit of this paper, to be intended as a sequel of the previous one about pantographic metamaterials [CMAT1], was to present an overview on all new advances in the different fields linked to the study of pantographic structures. In particular, we have shown (i) how the recently developed 3D printing techniques have made possible the production of many of the objects which were only theoretically but not factually designed. We have highlighted (ii) the variety of experiments which is nowadays available to test developed theoretical models. Indeed, beyond standard tests like Bias extension and shear, newly conceived tests like torsion, fiber extraction and dynamical measurements have been addressed for pantograhic fabrics. We have shown that (iii) an important tool in the study of pantographic structures is represented by image analysis techniques.

Regarding improovements in manufacturing of pantographic structures, the importance of technological developments has been emphatically remarked mainly in the case of metallic pantographic structures with (quasi-)perfect pivots and for micro pantographic structures. Furthermore, a fundamental advantage of rapid prototyping techniques consists in that the same CAD file used for the fabrication of the sample can be also used to perform full-scale 3D numerical simulations using Cauchy continua: this allows for an optimised experiment design.

Acknowledgments

Mario Spagnuolo has received funding from the European Union's Horizon 2020 research and innovation programme under the Marie Skłodowska-Curie grant agreement No 665850.

Anil Misra is funded by United States National Science Foundation (NSF) grant CMMI-1727433.

The author Christian Hesch gratefully acknowledge the support of the Deutsche Forschungsgemeinschaft (DFG) under grant HE5943/8-1 and DI2306/1-1. The author Sofia Hesch gratefully acknowledge the help of Heiko Bendler at the Institute of Mechanics at the Karlsruhe Institute of Technology (KIT) to perform the experimental investigations on organic sheets. The author Sofia Hesch also thanks Tamara Reinicke for supporting the investigations at the Chair of Product Development at the University of Siegen.

References

1. F. dell'Isola, G. Maier, U. Perego, U. Andreaus, R. Esposito, and S. Forest, "The complete works of Gabrio Piola: volume I," *Cham, Switzerland: Springer*, 2014.
2. F. dell'Isola, U. Andreaus, and L. Placidi, "At the origins and in the vanguard of peridynamics, non-local and higher-gradient continuum mechanics: An underestimated and still topical contribution of Gabrio Piola," *Mathematics and Mechanics of Solids*, vol. 20, no. 8, pp. 887–928, 2015.

3. P. Germain, "La méthode des puissances virtuelles en mécanique des milieux continus. première partie: théorie du second gradient," *J. Mécanique*, vol. 12, pp. 236–274, 1973.
4. P. Germain, "The method of virtual power in continuum mechanics. part 2: Microstructure," *SIAM Journal on Applied Mathematics*, vol. 25, no. 3, pp. 556–575, 1973.
5. R. D. Mindlin, "Micro-structure in linear elasticity," *Archive for Rational Mechanics and Analysis*, vol. 16, no. 1, pp. 51–78, 1964.
6. R. D. Mindlin, "Second gradient of strain and surface-tension in linear elasticity," *International Journal of Solids and Structures*, vol. 1, no. 4, pp. 417–438, 1965.
7. R. D. Mindlin and N. Eshel, "On first strain-gradient theories in linear elasticity," *International Journal of Solids and Structures*, vol. 4, no. 1, pp. 109–124, 1968.
8. R. A. Toupin, "Theories of elasticity with couple-stress," *Archive for Rational Mechanics and Analysis*, vol. 17, no. 2, pp. 85–112, 1964.
9. L. Sedov, "Variational methods of constructing models of continuous media," in *Irreversible aspects of continuum mechanics and transfer of physical characteristics in moving fluids*, pp. 346–358, Springer, 1968.
10. J. Altenbach, H. Altenbach, and V. A. Eremeyev, "On generalized cosserat-type theories of plates and shells: a short review and bibliography," *Archive of Applied Mechanics*, vol. 80, no. 1, pp. 73–92, 2010.
11. V. A. Eremeyev, "On the material symmetry group for micromorphic media with applications to granular materials," *Mechanics Research Communications*, vol. 94, pp. 8–12, 2018.
12. V. A. Eremeyev, G. Rosi, and S. Naili, "Comparison of anti-plane surface waves in strain-gradient materials and materials with surface stresses," *Mathematics and Mechanics of Solids*, p. 1081286518769960.
13. V. A. Eremeyev and F. dell'Isola, "A note on reduced strain gradient elasticity," in *Generalized Models and Non-classical Approaches in Complex Materials 1*, pp. 301–310, Springer, 2018.
14. F. dell'Isola, P. Seppecher, J. J. Alibert, T. Lekszycki, R. Grygoruk, M. Pawlikowski, D. Steigmann, I. Giorgio, U. Andreaus, E. Turco, *et al.*, "Pantographic metamaterials: an example of mathematically driven design and of its technological challenges," *Continuum Mechanics and Thermodynamics*, pp. 1–34.
15. F. dell'Isola, I. Giorgio, M. Pawlikowski, and N. Rizzi, "Large deformations of planar extensible beams and pantographic lattices: heuristic homogenization, experimental and numerical examples of equilibrium," *Proc. R. Soc. A*, vol. 472, no. 2185, p. 20150790, 2016.
16. M. Golaszewski, R. Grygoruk, I. Giorgio, M. Laudato, and F. Di Cosmo, "Metamaterials with relative displacements in their microstructure: technological challenges in 3d printing, experiments and numerical predictions," *Continuum Mechanics and Thermodynamics*, pp. 1–20, 2018.
17. P. Casal, "La capillarité interne," *Cahier du groupe Français de rhéologie, CNRS VI*, vol. 3, pp. 31–37, 1961.
18. P. Casal, "Theory of second gradient and capillarity," *COMPTES RENDUS HEBDOMADAIRES DES SEANCES DE L ACADEMIE DES SCIENCES SERIE A*, vol. 274, no. 22, p. 1571, 1972.
19. P. Seppecher, J.-J. Alibert, and F. dell'Isola, "Linear elastic trusses leading to continua with exotic mechanical interactions," in *Journal of Physics: Conference Series*, vol. 319, p. 012018, IOP Publishing, 2011.
20. J.-J. Alibert, P. Seppecher, and F. Dell'Isola, "Truss modular beams with deformation energy depending on higher displacement gradients," *Mathematics and Mechanics of Solids*, vol. 8, no. 1, pp. 51–73, 2003.
21. A. Misra, T. Lekszycki, I. Giorgio, G. Ganzosch, W. H. Müller, and F. dell'Isola, "Pantographic metamaterials show atypical poynting effect reversal," *Mechanics Research Communications*, vol. 89, pp. 6–10, 2018.
22. E. Barchiesi, G. Ganzosch, C. Liebold, L. Placidi, R. Grygoruk, and W. H. Müller, "Out-of-plane buckling of pantographic fabrics in displacement-controlled shear tests: experimental results and model validation," *Continuum Mechanics and Thermodynamics*, pp. 1–13.

23. S. Morville, M. Carin, P. Peyre, M. Gharbi, D. Carron, P. Le Masson, and R. Fabbro, "2d longitudinal modeling of heat transfer and fluid flow during multilayered direct laser metal deposition process," *Journal of Laser Applications*, vol. 24, no. 3, p. 032008, 2012.
24. T. Vilaro, V. Kottman-Rexerodt, M. Thomas, C. Colin, P. Bertrand, L. Thivillon, S. Abed, V. Ji, P. Aubry, P. Peyre, *et al.*, "Direct fabrication of a ti-47al-2cr-2nb alloy by selective laser melting and direct metal deposition processes," in *Advanced Materials Research*, vol. 89, pp. 586–591, Trans Tech Publ, 2010.
25. V. Gunenthiram, P. Peyre, M. Schneider, M. Dal, F. Coste, and R. Fabbro, "Analysis of laser–melt pool–powder bed interaction during the selective laser melting of a stainless steel," *Journal of Laser Applications*, vol. 29, no. 2, p. 022303, 2017.
26. O. Andreau, I. Koutiri, P. Peyre, J.-D. Penot, N. Saintier, E. Pessard, T. De Terris, C. Dupuy, and T. Baudin, "Texture control of 316l parts by modulation of the melt pool morphology in selective laser melting," *Journal of Materials Processing Technology*, vol. 264, pp. 21–31, 2019.
27. D. Zhang, *Entwicklung des selective laser melting (SLM) für Aluminiumwerkstoffe*. Shaker, 2004.
28. N. Keller and V. Ploshikhin, "New method for fast predictions of residual stress and distortion of am parts," in *Solid Freeform Fabrication Symposium (SFF), Austin, TX, Aug*, pp. 4–6, 2014.
29. H. N. Chia and B. M. Wu, "Recent advances in 3d printing of biomaterials," *Journal of biological engineering*, vol. 9, no. 1, p. 4, 2015.
30. S. Bhashyam, K. Hoon Shin, and D. Dutta, "An integrated cad system for design of heterogeneous objects," *Rapid Prototyping Journal*, vol. 6, no. 2, pp. 119–135, 2000.
31. A. C. Fischer, M. Mäntysalo, and F. Niklaus, "Inkjet printing, laser-based micromachining and micro 3d printing technologies for mems," in *Handbook of Silicon Based MEMS Materials and Technologies (Second Edition)*, pp. 550–564, Elsevier, 2015.
32. M. Malinauskas, A. Žukauskas, S. Hasegawa, Y. Hayasaki, V. Mizeikis, R. Buividas, and S. Juodkazis, "Ultrafast laser processing of materials: from science to industry," *Light: Science & Applications*, vol. 5, no. 8, p. e16133, 2016.
33. I. Sakellari, E. Kabouraki, D. Gray, V. Purlys, C. Fotakis, A. Pikulin, N. Bityurin, M. Vamvakaki, and M. Farsari, "Diffusion-assisted high-resolution direct femtosecond laser writing," *Acs Nano*, vol. 6, no. 3, pp. 2302–2311, 2012.
34. J. Combe, "Laser assisted writing of three-dimensional conductive nano-structure," *MS thesis, University of California, Berkeley, and Swiss Federal Institute of Technology (ETH), Zurich*, 2016.
35. K. Terzaki, N. Vasilantonakis, A. Gaidukeviciute, C. Reinhardt, C. Fotakis, M. Vamvakaki, and M. Farsari, "3d conducting nanostructures fabricated using direct laser writing," *Optical Materials Express*, vol. 1, no. 4, pp. 586–597, 2011.
36. A. P. Cote, A. I. Benin, N. W. Ockwig, M. O'keeffe, A. J. Matzger, and O. M. Yaghi, "Porous, crystalline, covalent organic frameworks," *science*, vol. 310, no. 5751, pp. 1166–1170, 2005.
37. F. Dell'Isola, M. Cuomo, L. Greco, and A. Della Corte, "Bias extension test for pantographic sheets: numerical simulations based on second gradient shear energies," *Journal of Engineering Mathematics*, vol. 103, no. 1, pp. 127–157, 2017.
38. D. Scerrato, I. A. Zhurba Eremeeva, T. Lekszycki, and N. L. Rizzi, "On the effect of shear stiffness on the plane deformation of linear second gradient pantographic sheets," *ZAMM-Journal of Applied Mathematics and Mechanics/Zeitschrift für Angewandte Mathematik und Mechanik*, vol. 96, no. 11, pp. 1268–1279, 2016.
39. E. Turco, F. Dell'Isola, N. L. Rizzi, R. Grygoruk, W. H. Müller, and C. Liebold, "Fiber rupture in sheared planar pantographic sheets: numerical and experimental evidence," *Mechanics Research Communications*, vol. 76, pp. 86–90, 2016.
40. G. Ganzosch, K. Hoschke, T. Lekszycki, I. Giorgio, E. Turco, and W. Müller, "3d-measurements of 3d-deformations of pantographic structures," *TECHNISCHE MECHANIK*, vol. 38, no. 3, pp. 233–245, 2018.
41. U. Andreaus, M. Spagnuolo, T. Lekszycki, and S. R. Eugster, "A ritz approach for the static analysis of planar pantographic structures modeled with nonlinear euler–bernoulli beams," *Continuum Mechanics and Thermodynamics*, pp. 1–21, 2018.

42. E. Turco, F. dell'Isola, A. Cazzani, and N. L. Rizzi, "Hencky-type discrete model for pantographic structures: numerical comparison with second gradient continuum models," *Zeitschrift für angewandte Mathematik und Physik*, vol. 67, no. 4, p. 85, 2016.
43. M. Spagnuolo, K. Barcz, A. Pfaff, F. dell'Isola, and P. Franciosi, "Qualitative pivot damage analysis in aluminum printed pantographic sheets: numerics and experiments," *Mechanics Research Communications*, vol. 83, pp. 47–52, 2017.
44. L. Placidi, L. Greco, S. Bucci, E. Turco, and N. L. Rizzi, "A second gradient formulation for a 2d fabric sheet with inextensible fibres," *Zeitschrift für angewandte Mathematik und Physik*, vol. 67, no. 5, p. 114, 2016.
45. E. Turco, A. Misra, M. Pawlikowski, F. dell'Isola, and F. Hild, "Enhanced piola-hencky discrete models for pantographic sheets with pivots without deformation energy: numerics and experiments," *International Journal of Solids and Structures*, 2018.
46. J. Bauer, A. Schroer, R. Schwaiger, I. Tesari, C. Lange, L. Valdevit, and O. Kraft, "Push-to-pull tensile testing of ultra-strong nanoscale ceramic–polymer composites made by additive manufacturing," *Extreme Mechanics Letters*, vol. 3, pp. 105–112, 2015.
47. H.-T. Lee, M.-S. Kim, G.-Y. Lee, C.-S. Kim, and S.-H. Ahn, "Shape memory alloy (sma)-based microscale actuators with 60% deformation rate and 1.6 khz actuation speed," *Small*, vol. 14, no. 23, p. 1801023, 2018.
48. A. Maggi, H. Li, and J. R. Greer, "Three-dimensional nano-architected scaffolds with tunable stiffness for efficient bone tissue growth," *Acta biomaterialia*, vol. 63, pp. 294–305, 2017.
49. F. Maurin, F. Greco, and W. Desmet, "Isogeometric analysis for nonlinear planar pantographic lattice: discrete and continuum models," *Continuum Mechanics and Thermodynamics*, pp. 1–14.
50. G. Capobianco, S. R. Eugster, and T. Winandy, "Modeling planar pantographic sheets using a nonlinear euler–bernoulli beam element based on b-spline functions," *PAMM*, vol. 18, no. 1, pp. 1–2, 2018.
51. J. A. Cottrell, T. J. Hughes, and Y. Bazilevs, *Isogeometric analysis: toward integration of CAD and FEA*. John Wiley & Sons, 2009.
52. J. Kiendl, K.-U. Bletzinger, J. Linhard, and R. Wüchner, "Isogeometric shell analysis with kirchhoff–love elements," *Computer Methods in Applied Mechanics and Engineering*, vol. 198, no. 49-52, pp. 3902–3914, 2009.
53. F. Maurin, L. Dedè, and A. Spadoni, "Isogeometric rotation-free analysis of planar extensible-elastica for static and dynamic applications," *Nonlinear Dynamics*, vol. 81, no. 1-2, pp. 77–96, 2015.
54. L. Greco and M. Cuomo, "B-spline interpolation of kirchhoff-love space rods," *Computer Methods in Applied Mechanics and Engineering*, vol. 256, pp. 251–269, 2013.
55. M. Cuomo and L. Greco, "An implicit strong G^1-conforming formulation for the analysis of the kirchhoff plate model," *Continuum Mechanics and Thermodynamics*, pp. 1–25.
56. L. Greco, M. Cuomo, and L. Contrafatto, "A reconstructed local b formulation for isogeometric kirchhoff–love shells," *Computer Methods in Applied Mechanics and Engineering*, vol. 332, pp. 462–487, 2018.
57. L. Greco, M. Cuomo, L. Contrafatto, and S. Gazzo, "An efficient blended mixed b-spline formulation for removing membrane locking in plane curved kirchhoff rods," *Computer Methods in Applied Mechanics and Engineering*, vol. 324, pp. 476–511, 2017.
58. A. Cazzani, M. Malagù, and E. Turco, "Isogeometric analysis of plane-curved beams," *Mathematics and Mechanics of Solids*, vol. 21, no. 5, pp. 562–577, 2016.
59. A. Cazzani, M. Malagù, E. Turco, and F. Stochino, "Constitutive models for strongly curved beams in the frame of isogeometric analysis," *Mathematics and Mechanics of Solids*, vol. 21, no. 2, pp. 182–209, 2016.
60. A. Cazzani, M. Malagù, and E. Turco, "Isogeometric analysis: a powerful numerical tool for the elastic analysis of historical masonry arches," *Continuum Mechanics and thermodynamics*, vol. 28, no. 1-2, pp. 139–156, 2016.
61. A. Cazzani, F. Stochino, and E. Turco, "An analytical assessment of finite element and isogeometric analyses of the whole spectrum of timoshenko beams," *ZAMM-Journal of Applied Mathematics and Mechanics/Zeitschrift für Angewandte Mathematik und Mechanik*, vol. 96, no. 10, pp. 1220–1244, 2016.

62. Y. Rahali, I. Giorgio, J. Ganghoffer, and F. Dell'Isola, "Homogenization à la Piola produces second gradient continuum models for linear pantographic lattices," *International Journal of Engineering Science*, vol. 97, pp. 148–172, 2015.
63. M. Laudato, L. Manzari, E. Barchiesi, F. Di Cosmo, and P. Göransson, "First experimental observation of the dynamical behavior of a pantographic metamaterial," *Mechanics Research Communications*, 2018.
64. V. Research, "Phantom Ultrahigh-Speed Cameras UHS-12 Series Manual," July 2017.
65. Nikon, "AF Micro-Nikkor 200mm f/4d IF-ED from Nikon," June 2017.
66. LaVision GmbH, *Product-Manual for DaVis 8.3: Imaging Tools*. LaVision GmbH, June 2015. Document name: 1003012_ImagingTools_D83.pdf.
67. P. Franciosi, M. Spagnuolo, and O. U. Salman, "Mean Green operators of deformable fiber networks embedded in a compliant matrix and property estimates," *Continuum Mechanics and Thermodynamics*, pp. 1–32, 2018.
68. P. Franciosi and G. Lormand, "Using the radon transform to solve inclusion problems in elasticity," *International Journal of Solids and Structures*, vol. 41, no. 3-4, pp. 585–606, 2004.
69. P. Franciosi, "On the modified Green operator integral for polygonal, polyhedral and other non-ellipsoidal inclusions," *International Journal of Solids and Structures*, vol. 42, no. 11-12, pp. 3509–3531, 2005.
70. P. Franciosi, "A decomposition method for obtaining global mean Green operators of inclusions patterns. application to parallel infinite beams in at least transversally isotropic media," *International Journal of Solids and Structures*, 2018.
71. P. Harrison, M. F. Alvarez, and D. Anderson, "Towards comprehensive characterisation and modelling of the forming and wrinkling mechanics of engineering fabrics," *International Journal of Solids and Structures*, vol. 154, pp. 2–18, 2018.
72. I. Giorgio, P. Harrison, F. Dell'Isola, J. Alsayednoor, and E. Turco, "Wrinkling in engineering fabrics: a comparison between two different comprehensive modelling approaches," *Proceedings of the Royal Society A: Mathematical, Physical and Engineering Sciences*, vol. 474, no. 2216, p. 20180063, 2018.
73. P. Harrison, "Modelling the forming mechanics of engineering fabrics using a mutually constrained pantographic beam and membrane mesh," *Composites Part A: Applied Science and Manufacturing*, vol. 81, pp. 145–157, 2016.
74. M. Cima, E. Sachs, L. Cima, J. Yoo, S. Khanuja, S. Borland, B. Wu, and R. Giordano, "Computer-derived microstructures by 3d printing: bio-and structural materials," in *Solid Freeform Fabr Symp Proc: DTIC Document*, pp. 181–90, 1994.
75. I. Giorgio, U. Andreaus, T. Lekszycki, and A. D. Corte, "The influence of different geometries of matrix/scaffold on the remodeling process of a bone and bioresorbable material mixture with voids," *Mathematics and Mechanics of Solids*, vol. 22, no. 5, pp. 969–987, 2017.
76. M. Sutton, J. Orteu, and H. Schreier, *Image correlation for shape, motion and deformation measurements: basic concepts, theory and applications*. Springer Science & Business Media, 2009.
77. F. Hild and S. Roux, "Digital image correlation," in *Optical Methods for Solid Mechanics. A Full-Field Approach* (P. Rastogi and E. Hack, eds.), (Weinheim (Germany)), pp. 183–228, Wiley-VCH, 2012.
78. F. Hild and S. Roux, "Comparison of local and global approaches to digital image correlation," *Experimental Mechanics*, vol. 52, no. 9, pp. 1503–1519, 2012.
79. Z. Tomičević, F. Hild, and S. Roux, "Mechanics-aided digital image correlation," *The Journal of Strain Analysis for Engineering Design*, vol. 48, no. 5, pp. 330–343, 2013.
80. C. Geuzaine and J.-F. Remacle, "Gmsh: A 3-D finite element mesh generator with built-in pre- and post-processing facilities," *International Journal for Numerical Methods in Engineering*, vol. 79, no. 11, pp. 1309–1331, 2009.